

QUANTITATIVE SPECTROSCOPY OF BLUE SUPERGIANT STARS IN THE DISK OF M81: METALLICITY, METALLICITY GRADIENT, AND DISTANCE

ROLF-PETER KUDRITZKI^{1,4,5}, MIGUEL A. URBANEJA¹, ZACHARY GAZAK¹, FABIO BRESOLIN¹, NORBERT PRZYBILLA²,
WOLFGANG GIEREN³, AND GRZEGORZ PIETRZYŃSKI^{3,6}

¹ Institute for Astronomy, University of Hawaii, 2680 Woodlawn Drive, Honolulu, HI 96822, USA; kud@ifa.hawaii.edu, urbaneja@ifa.hawaii.edu, zgazak@ifa.hawaii.edu, bresolin@ifa.hawaii.edu

² Dr. Remeis-Sternwarte Bamberg & ECAP, D-96049 Bamberg, Germany; przybilla@sternwarte.uni-erlangen.de

³ Departamento de Astronomia, Universidad de Concepcion, Casilla 160-C, Concepcion, Chile; wgieren@astro-udec.cl, pietrzyn@astrouw.edu.pl

Received 2011 September 27; accepted 2011 December 15; published 2012 February 9

ABSTRACT

The quantitative spectral analysis of low-resolution ($\sim 5 \text{ \AA}$) Keck LRIS spectra of blue supergiants in the disk of the giant spiral galaxy M81 is used to determine stellar effective temperatures, gravities, metallicities, luminosities, interstellar reddening, and a new distance using the flux-weighted gravity–luminosity relationship. Substantial reddening and extinction are found with $E(B - V)$ ranging between 0.13 and 0.38 mag and an average value of 0.26 mag. The distance modulus obtained after individual reddening corrections is 27.7 ± 0.1 mag. The result is discussed with regard to recently measured tip of the red giant branch and Cepheid distances. The metallicities (based on elements such as iron, titanium, magnesium) are supersolar (≈ 0.2 dex) in the inner disk ($R \lesssim 5$ kpc) and slightly subsolar (≈ -0.05 dex) in the outer disk ($R \gtrsim 10$ kpc) with a shallow metallicity gradient of $0.034 \text{ dex kpc}^{-1}$. The comparison with published oxygen abundances of planetary nebulae and metallicities determined through fits of *Hubble Space Telescope* color–magnitude diagrams indicates a late metal enrichment and a flattening of the abundance gradient over the last 5 Gyr. This might be the result of gas infall from metal-rich satellite galaxies. Combining these M81 metallicities with published blue supergiant abundance studies in the Local Group and the Sculptor Group, a galaxy mass–metallicity relationship based solely on stellar spectroscopic studies is presented and compared with recent studies of Sloan Digital Sky Survey star-forming galaxies.

Key words: galaxies: distances and redshifts – galaxies: individual (M81) – stars: abundances – stars: early-type

Online-only material: color figures

1. INTRODUCTION

The determination of the chemical composition and distances of galaxies is crucial for constraining the theory of galaxy formation and evolution in a dark energy and cold dark matter dominated universe. Ultimately, these measurements lead to ever-stronger constraints on the cosmological parameters and the history of cosmic chemical enrichment, from the primordial metal-free universe to the present-day chemically diversified structure. For instance, the relationship between central metallicity and galactic mass appears to be a Rosetta stone to understand chemical evolution and galaxy formation (Lequeux et al. 1979; Tremonti et al. 2004; Maiolino et al. 2008). In a similar way, the observed metallicity gradients in spiral galaxies, apparently large for spirals of lower mass and shallow for high-mass galaxies (Garnett et al. 1997; Skillman 1998; Garnett 2004), provide crucial insight into galaxy formation and evolution. Both the observed mass–metallicity relationship and the abundance gradients are used to test the theoretical predictions of hierarchical clustering, galaxy formation, merging, infall, galactic winds, and variability of star formation activity and initial mass function obtained in the framework of a Λ CDM-dominated universe (Prantzos & Boissier 2000; Naab & Ostriker 2006; Colavitti et al. 2008; Yin et al. 2009; Sánchez-

Blázquez et al. 2009; De Lucia et al. 2004; de Rossi et al. 2007; Finlator & Davé 2008; Brooks et al. 2007; Köppen et al. 2007; Wiersma et al. 2009; Davé et al. 2011a, 2011b). Note that this is only a small selection of papers relevant to the subject; others are found in the references therein.

However, as intriguing as the observations of the mass–metallicity relationship and the metallicity gradients of galaxies are, the published results are highly uncertain. They rely on observations of H II region emission lines, mostly restricted to oxygen, and the analysis method applied is the so-called strong-line method, which uses the fluxes of the strongest forbidden lines of (most commonly) [O II] and [O III] relative to H β . Unfortunately, abundances obtained with the strong-line method depend heavily on the calibration used. As a striking example, Kewley & Ellison (2008) have demonstrated that the quantitative shape of the mass–metallicity relationship of galaxies can change from very steep to almost flat depending on the calibration used. In the same way, as shown by Kudritzki et al. (2008) and Bresolin et al. (2009) in their study of the Sculptor spiral galaxy NGC 300, metallicity gradients of spiral galaxies can change from steep to flat and absolute values of metallicity can shift by as much as 0.6 dex, again as the result of different calibrations of the strong-line method. In consequence, galaxy metallicities are uncertain by 0.6–0.8 dex because of the systematic uncertainties inherent in the strong-line methods used. This major problem requires a fresh approach and is begging for the development of a new and independent method less affected by systematic uncertainties.

An obvious alternative method to constrain metallicity is the detailed quantitative spectroscopic analysis of individual blue

⁴ Also at: Max-Planck-Institute for Astrophysics, Karl-Schwarzschild-Str.1, D-85741 Garching, Germany.

⁵ Also at: University Observatory Munich, Scheinerstr. 1, D-81679 Munich, Germany.

⁶ Also at: Warsaw University Observatory, Al. Ujazdowskie 4, 00-478 Warsaw, Poland.

supergiant stars (BSGs) in galaxies. BSGs of spectral type A and B are massive stars in the mass range between 12 and 40 M_{\odot} in the short-lived evolutionary phase (10^3 to 10^5 years) when they leave the hydrogen main sequence and cross the H-R diagram (HRD) at constant luminosity and almost constant mass to become red supergiants. Because of Wien's law, massive stars increase their brightness in visual light dramatically when evolving toward lower temperatures and reach absolute visual magnitudes up to $M_V \approx -9.5$ mag in the BSG phase (Bresolin 2003), rivaling the integrated light of globular clusters and dwarf galaxies. Because of their extreme brightness, they are ideal tools to accurately determine the chemical composition of young stellar populations in galaxies.

BSG spectra are rich in metal absorption lines from several elements (C, N, O, Mg, Al, S, Si, Ti, Fe, among others). As young objects with ages of 10 Myr, they provide important probes of the current composition of the interstellar medium. Based on detailed high-resolution, very high signal-to-noise ratio (S/N) studies of BSGs, which yield abundances as accurate as 0.05 dex (Przybilla et al. 2006, 2008b; Schiller & Przybilla 2008), Kudritzki et al. (2008) developed an efficient new spectral diagnostic technique for low-resolution spectra (FWHM ~ 5 Å) with good S/N (50 or better), which allows for an accurate determination of effective temperature, gravity, metallicity, interstellar reddening, and extinction. Metallicities accurate to 0.1–0.2 dex for each individual target can be obtained at this lower resolution and S/N. The method has been applied to irregular and spiral galaxies in the Local Group (WLM, Bresolin et al. 2006; Urbaneja et al. 2008; NGC 3109, Evans et al. 2007; IC 1613, Bresolin et al. 2007; M33, U et al. 2009) and beyond (NGC 300, Kudritzki et al. 2008).

In this paper, we present the spectral analysis of low-resolution Keck LRIS spectra of 26 BSGs in the disk of the giant spiral galaxy M81. M81 is one of the most massive spirals in the Local Volume (McCommas et al. 2009). It has low foreground extinction with a galactic luminosity of $2.5L_*$ (corresponding to $M_K = -24$ mag and $M_{K^*} = -23$ mag) and is characteristic of disk galaxies seen at redshift surveys out to $z \sim 1$ (Williams et al. 2009). The star formation history and chemical evolution of this galaxy have been subject to extensive recent photometric studies (Dalcanton et al. 2009; Davidge 2009; Williams et al. 2009; Barker et al. 2009; Durrell et al. 2010). H II regions and planetary nebulae (PNe) have been studied by Stanghellini et al. (2010), extending the classical work by Garnett & Shields (1987) and Stauffer & Bothun (1984). With our work we provide for the first time direct quantitative spectroscopic information about stellar metallicity of the young disk population.

An important additional aspect of the quantitative spectroscopy of BSGs is their use as accurate distance indicators through the flux-weighted gravity–luminosity relationship (FGLR). This new distance determination method has been introduced by Kudritzki et al. (2003) and Kudritzki et al. (2008). It uses stellar gravity and effective temperature as a measure of absolute bolometric magnitude and provides a distance estimate that is free of the uncertainties caused by interstellar reddening, since the determination of reddening is a by-product of the quantitative spectral analysis. First distance determinations using this method have been carried out by Urbaneja et al. (2008, WLM) and U et al. (2009, M33).

There has been a long history of attempts to measure the distance to M81 from Hubble (1929) to the present (see McCommas et al. 2009 for references and a plot of distance modulus as a function of time). The work published over

the last decade gives a range between 27.60 and 28.03 mag in distance modulus, indicating an uncertainty of 20%. Our BSG spectroscopy and the effective temperatures and gravities determined will give us an FGLR distance, which we can then compare with most recent *Hubble Space Telescope* (HST) work on Cepheids and the tip of the red giant branch (TRGB). M81 has been used as one of the calibration galaxies for the Tully–Fisher and the surface fluctuation methods in the HST Key Project (Freedman et al. 2001) and by Mould & Sakai (2008, 2009).

In Section 2, we describe the observations and data reduction. Section 3 discusses the quantitative spectroscopic analysis and the determination of extinction, effective temperature, gravity, and metallicity. Sections 4 and 5 discuss interstellar reddening and compare the spectroscopically determined stellar parameters with evolutionary tracks in order to constrain the evolutionary status of the objects observed. Section 6 compares metallicity and metallicity gradient of the BSGs with published metallicity constraints for the older disk population of M81 and discusses chemical evolution over the last Gyrs. In Section 7, we provide a galaxy mass–metallicity relationship based on BSG spectroscopic studies and compare with published work using H II region emission lines. In Section 8, we determine a new distance to M81 using the FGLR method and discuss recent Cepheid and TRGB work. Section 9 summarizes the results and discusses aspects of future work.

2. OBSERVATIONS AND DATA REDUCTION

The observations were carried out with the Keck 1 telescope on Mauna Kea and the Low Resolution Imaging Spectrograph (LRIS; Oke et al. 1995) using the atmospheric dispersion corrector, a slit width of 1.2 arcsec, the D560 dichroic, and the 600/4000 grism (0.63 Å pixel $^{-1}$) and the 900/5500 grating (0.53 Å pixel $^{-1}$) in the blue and red channel, respectively. In this paper, we will discuss and analyze the blue channel (LRIS-B) spectra only, which have a resolution of 5 Å FWHM. Because of the UV sensitivity of the LRIS-B configuration, the spectra extend to shortward of the Balmer discontinuity at 3640 Å, which is crucial for the determination of T_{eff} from the Balmer jump (see Section 3). Three MOS fields were prepared with 20 to 25 targets each. The BSG candidate targets were selected from HST Advanced Camera for Surveys (ACS) B , V images obtained within the ANGST project (Dalcanton et al. 2009), which covers the whole galaxy. Published B , V photometry of the M81 ANGST fields was used to preselect targets with -0.2 mag $\lesssim B - V \lesssim 0.4$ mag and $V \lesssim 21.5$ mag. Each target was carefully inspected with regard to multiplicity. Figure 1 shows the selection from the color–magnitude diagram (CMD) and the location of our targets within the galaxy. None of our targets are related to one of the stellar clusters investigated by Chandar et al. (2001) or Santiago-Cortés et al. (2010).

The observations were scheduled for three dark nights in 2010 (February 14–16). The first night had perfect conditions with 0.75 arcsec seeing, yielding reasonably exposed spectra with a total exposure time of 6.75 hr (observed in exposure segments of 45 minutes each) of the first field (field Z). The observing conditions degraded significantly during the second and third nights with poor seeing (1.3 arcsec) and occasional clouds. As a result, almost one-half of these two nights was lost and only one additional field (field C) could be observed with a total of 11.3 hr exposure time under mediocre conditions.

Data reduction was performed using a custom pipeline written in IDL designed to efficiently extract faint objects observed

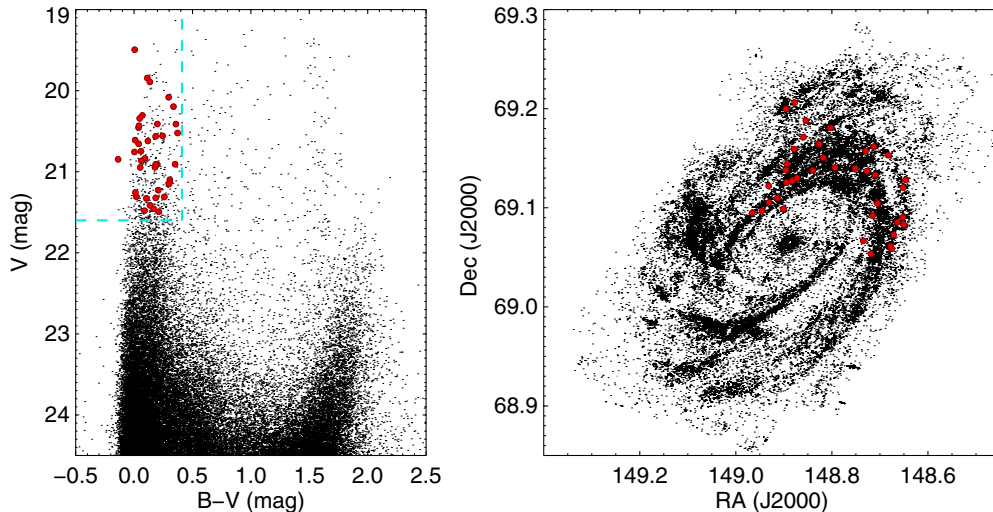


Figure 1. Selection of M81 BSG targets. Left: color-magnitude diagram (photometry from Dalcanton et al. 2009) with selection box (blue dashed) and selected targets (red). Right: location of selected targets within M81.

(A color version of this figure is available in the online journal.)

over a full night. LRIS science and calibration frames were flat fielded and bias subtracted. For each reduced frame, object spectra were traced along the dispersion axis and extracted using the optimal extraction method (Horne 1986) meant to maximize the S/N of faint spectra. For this technique we utilized a Moffat function, which was determined to best fit the two-dimensional spectral profile at each pixel (wavelength) perpendicular to the dispersion. The Moffat fit was modified to include a measure of the background level for subtraction. The spectra were then wavelength calibrated using techniques in the `idlspec2d` IDL package developed for Sloan Digital Sky Survey (SDSS).

Each science object spectrum was flux calibrated by performing corrections for wavelength-dependent extinction at varying airmass over Mauna Kea (Bèland et al. 1988) and then multiplying by a sensitivity function to convert extracted data numbers into units of $\text{erg/s/cm}^2/\text{\AA}$. The sensitivity function was calculated by scaling airmass-corrected observed flux standard stars (GD 50, Feige 34, HZ 44, and BD +33°2642) to the published spectral energy distributions (SEDs) of Oke (1990). A final spectrum for each target was produced by taking the median of all wavelength- and flux-calibrated spectral frames. Those spectra were normalized by manually selecting continuum regions and dividing by a high-order polynomial fit to the continuum flux levels. The S/N values of our spectra vary between 40 and 80.

Table 1 provides the information about the objects used for this spectroscopic study. While we selected 25 targets in each field, we could not use all of them. A few turned out to be blue foreground objects in the Milky Way halo, some had composite spectra indicating the presence of several objects in the slit, and for some the S/N was not sufficient. For the remaining objects we list coordinates, galactocentric distance, spectral type, V magnitude, $B - V$ color, and the measured Balmer jump D_B in Table 1. The way that D_B is defined and measured is described in Kudritzki et al. (2008).

3. SPECTROSCOPIC ANALYSIS

The analysis method has been described in detail in Kudritzki et al. (2008). A comprehensive grid of line-blanketed model atmospheres and very detailed NLTE line formation calculations is used to calculate SEDs, including the Balmer jump, and

normalized synthetic spectra. Relative to the work presented in Kudritzki et al. (2008), the grid has been extended to cover temperatures from 16,000 K down to 7900 K at gravities between $\log g = 3.0$ and 0.8 (cgs). The lower limit of $\log g$ is a function of T_{eff} parallel to the Eddington limit. Models are calculated for 14 metallicities $[Z] = \log(Z/Z_{\odot})$: $-1.30, -1.15, -1.00, -0.85, -0.70, -0.60, -0.50, -0.40, -0.30, -0.15, 0.00, 0.15, 0.30, 0.50$ dex. Z/Z_{\odot} is the metallicity relative to the Sun in the sense that the abundance for each element is scaled by the same factor relative to its solar abundance. Solar abundances were taken from Grevesse & Sauval (1998), except for oxygen, where we adopt the value from Allende Prieto et al. (2001). For all further details of the model grid we refer the reader to Kudritzki et al. (2008). The physics of the model atmospheres and the NLTE line formation calculations are described in detail by Przybilla et al. (2006) and references therein.

The spectral analysis proceeds in several steps. First, fit curves in the $(\log g, T_{\text{eff}})$ -plane are constructed, along which the models reproduce the observed Balmer jump and the Balmer lines. The Balmer jump is mostly a function of temperature but also depends weakly on gravity, whereas the Balmer lines depend mostly on gravity and weakly on temperature. Figures 2 and 3 demonstrate the dependence of the Balmer jump on temperature and of the Balmer lines on gravity. The intersection area of these fit curves determines the stellar effective temperatures and gravities and the corresponding uncertainties (see Figure 4). The fact that the fit curves for the Balmer jump and the Balmer lines are not orthogonal leads to relatively large error boxes, in particular with regard to gravity $\log g$. On the other hand, the flux-weighted gravity

$$\log g_F = \log g - 4 \log(T_{\text{eff}} \times 10^{-4}) \quad (1)$$

is determined much more accurately, since the Balmer lines depend solely on $\log g_F$ for temperatures higher than 9000 K (for an explanation of the physics behind this behavior, see Kudritzki et al. 2008). This is important for the use of flux-weighted gravity as an indicator of absolute magnitude and distance (see Section 8). Figures 5–8 show fits of D_B and one Balmer line for the remaining objects in Table 1 (with spectral types later than or equal to B3) to give an impression of the

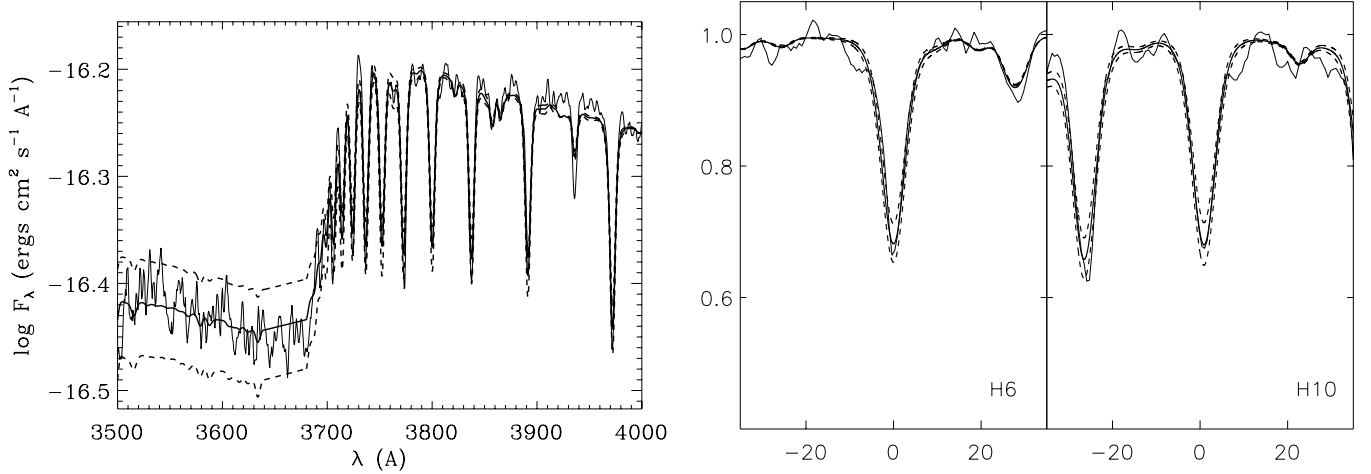


Figure 2. Analysis of object Z10. Left: fit of the observed Balmer jump. The final model with the parameters given in Table 2 (thick solid curve) fits the Balmer discontinuity well. Two models with T_{eff} higher/lower by 500 K are also shown (dashed) to demonstrate the temperature sensitivity of the D_B fit. Right: fit of two Balmer lines with the final model. Two models with $\log g$ higher/lower by 0.1 dex are shown (dashed) to demonstrate the gravity sensitivity of the Balmer line fits. Note that the strong spectral line at the left edge of the panel for H₁₀ is H₁₁, which is not used for the fits, because it is at the edge of the normalized spectrum, where continuum rectification becomes difficult.

Table 1
M81–Spectroscopic Targets

No.	Name	α_{2000} (h m s)	δ_{2000} ($^{\circ}$ ' ")	R/R_{25}^a	sp.t.	m_V (mag)	$B - V$ (mag)	D_B (dex)	(10)
(1)	(2)	(3)	(4)	(5)	(6)	(7)	(8)	(9)	
0	Z1	9 55 30.580	69 12 22.716	0.83	B7	20.946	0.052	0.126	
1	Z2	9 55 34.965	69 11 58.524	0.81	B4	21.493	0.011	0.084	
2	Z3	9 55 25.022	69 11 16.908	0.69	B7	20.847	0.093	0.122	
3	Z4	9 55 12.686	69 10 50.880	0.61	B9	20.305	0.198		b
4	Z5	9 55 26.224	69 10 16.896	0.60	B3	21.452	0.059	0.056	
5	Z6	9 55 18.204	69 09 51.984	0.53	B7	21.206	0.185	0.156	
6	Z7	9 55 30.948	69 09 33.696	0.55	A3	21.454	0.244	0.539	
7	Z9	9 55 10.488	69 08 27.132	0.41	A4	21.296	0.358		b
8	Z10	9 55 34.353	69 08 39.552	0.48	B9	21.236	0.185	0.230	
9	Z11	9 55 21.518	69 08 15.864	0.39	B1	21.327	0.048		
10	Z12	9 55 35.100	69 08 16.908	0.45	B4	21.020	0.185	0.049	
11	Z13	9 55 29.344	69 07 48.432	0.37	B1.5	21.113	0.113		
12	Z14	9 55 31.761	69 07 39.036	0.36	B7	21.371	0.207	0.127	
13	Z15	9 55 34.783	69 07 31.440	0.37	B0.5	20.495	0.136		
14	Z16	9 55 43.579	69 07 18.768	0.42	B4	19.979	0.135	0.002	
15	Z17	9 55 39.237	69 06 35.172	0.69	A4	21.165	0.372	0.586	
16	Z18	9 55 43.442	69 06 18.972	0.33	B9	20.402	0.211	0.171	
17	Z20	9 55 46.972	69 05 48.516	0.32	A1	20.330	0.305	0.110	
18	C6	9 54 35.976	69 05 00.168	0.74	A1	20.784	0.306	0.288	
19	C9	9 54 51.542	69 05 33.288	0.51	B6	21.217	0.071	0.129	
20	C11	9 54 49.214	69 06 17.640	0.53	B9	20.412	0.296	0.178	
21	C13	9 54 36.451	69 07 15.708	0.69	B2	21.152	0.038	0.015	
22	C14	9 54 35.196	69 07 43.752	0.70	B3	21.414	0.039	0.055	
23	C16	9 54 54.530	69 08 14.892	0.51	B9	21.245	0.337	0.186	
24	C20	9 54 51.079	69 09 43.992	0.60	B9	20.411	0.259	0.249	
25	C21	9 55 18.777	69 09 52.668	0.53	B8	20.395	0.105		b

Notes.

^a Galactocentric distance, in units of $R_{25} = 11.99$ arcmin ≈ 12.09 kpc (distance modulus 27.70 mag). A position angle P.A. = 157° , an inclination $i = 57^{\circ}$, and central coordinates $\alpha_{2000} = 9^{\text{h}}55^{\text{m}}33^{\text{s}}.2$, $\delta_{2000} = 69^{\circ}3'55''$ were assumed (Hyperleda database; Paturel et al. 2003).

^b No near the UV spectral coverage; no Balmer jump measured.

quality of the data. We note that we usually try to use all Balmer lines from H₄ to H₁₀ to constrain gravity. However, varying from star to star, we may encounter difficulties with individual Balmer lines. H₇, for instance, is many times corrupted by interstellar Ca II absorption. H₄, H₅, and even H₆ are sometimes affected by H II emission. Another problem are strong stellar winds, which can fill H₄ and H₅ with broad emission. Spectral flaws

by improper corrections of cosmic-ray hits may also affect line profiles. However, in general, we have more than one Balmer line per star to constrain gravity, usually three to four. For Figures 2, 6, 8, and 9 we have selected the best-fitting cases.

Three objects of our sample are of earlier spectral type (B0.5 to B1.5). For those, the Balmer jump is not a good temperature indicator. We use the ionization equilibrium of Si II, Si III, and

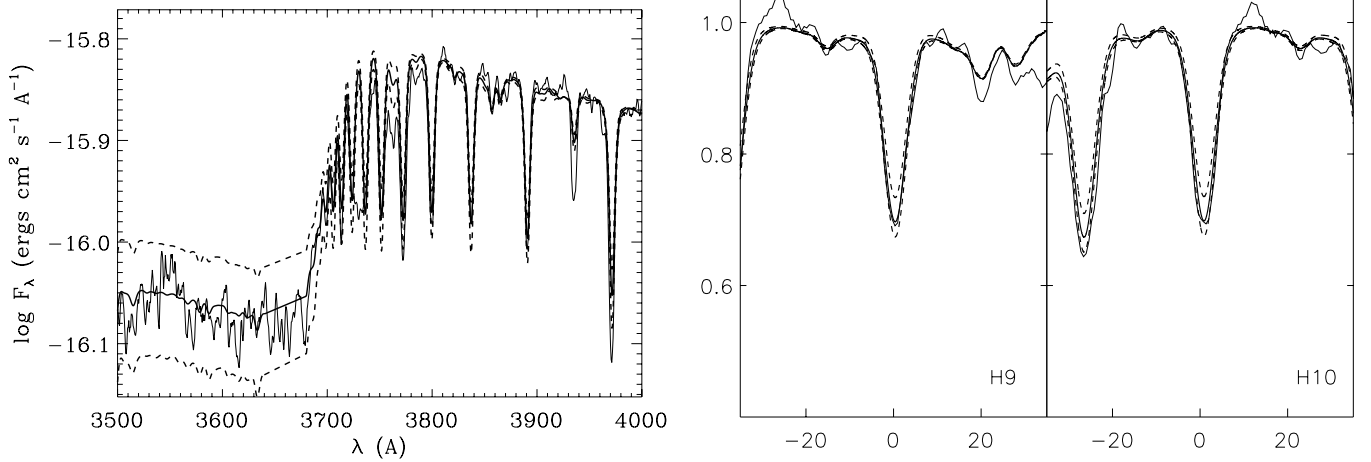
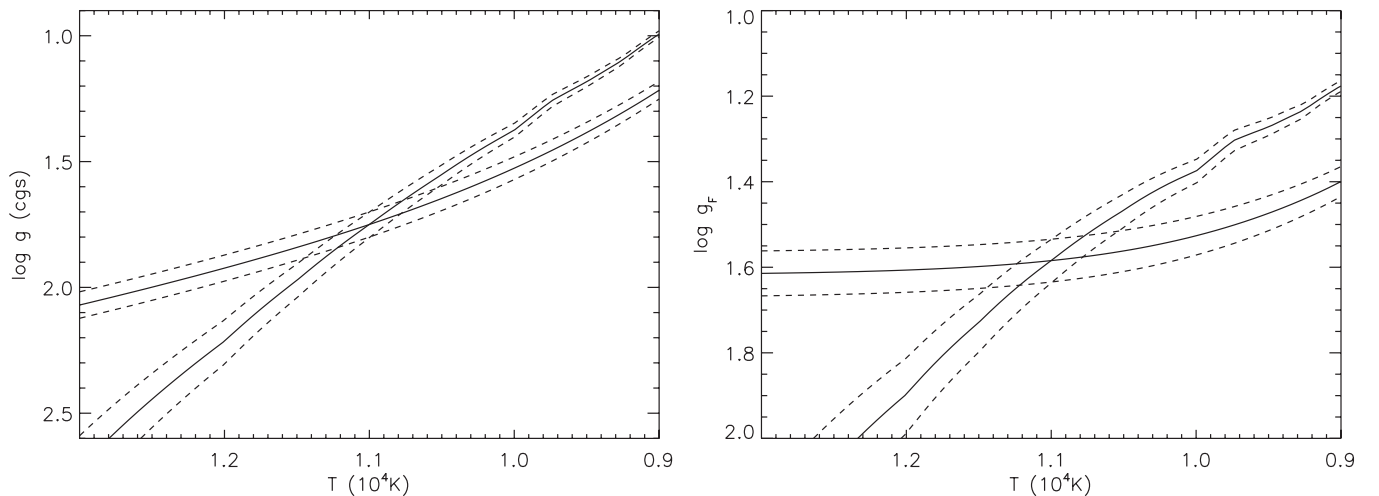


Figure 3. Same as Figure 2 but for object C20.

Figure 4. Fit diagrams for the fit of the Balmer jump (steeper curves) and the Balmer lines. Left: the $(\log g, T_{\text{eff}})$ diagram; right: $(\log g_F, T_{\text{eff}})$. T_{eff} is given in 10^4 K. The dashed curves indicate maximum errors of the fits. For discussion, see the text.

Si IV lines instead and apply the analysis method developed by Urbaneja et al. (2005a), which relies on the use of line-blanketed NLTE model atmospheres including the effects of stellar winds. Figure 9 shows the spectral fits for the key lines of these objects.

For three objects of later spectral type (Z4, Z9, C21) the wavelength range of the observed spectra does not cover the region of the Balmer jump. Thus, the only way to estimate their temperature is the relationship between effective temperature and spectral type (see Kudritzki et al. 2003). As shown by Kudritzki et al. (2008), this method works only as long as the metallicity is about solar. From the galactocentric distance of these objects and our study of metallicity and metallicity gradient (see Section 6) for the other objects in our sample this seems to be a reasonable assumption; thus, temperature, gravity, and luminosity of these objects are very likely well determined. Nevertheless, we will not make use of these objects for the determination of the distance to M81 from the flux-weighted gravity.

We note that with the fit of either the Balmer jump D_B , or the silicon equilibrium, or the spectral type in the $(\log g, T_{\text{eff}})$ -plane we can always calculate a reddening correction $E(B - V)$ along the fit curve at each effective temperature by comparing the observed value of $B - V$ with the one calculated by the

atmospheric model. For fitting the Balmer jump, we then correct for reddening using the Cardelli et al. (1989) reddening law with $R_V = 3.1$. Once we have found the intersection with the fit curve for the Balmer lines, we can then also determine the final reddening value $E(B - V)$ for the final values of T_{eff} and $\log g$. It is a big advantage of this spectroscopic determination of stellar parameters that it yields interstellar reddening for free. For an estimate of distances, this is a fundamental advantage of the method.

In the next step, with effective temperature and gravity measured we can use our synthetic spectra to determine metallicity. For this purpose, we concentrate on the objects cooler than 17,000 K, since the S/N is not high enough for the hotter objects (see Urbaneja et al. 2005a). Three of the cooler objects cannot be used for this purpose, because their effective temperature is not constrained by a Balmer jump measurement but by the use of the spectral type already assuming solar abundance. In addition, two more objects (Z11, C16) have spectra too noisy for a metallicity fit. Object Z20 shows a metal line spectrum at longer wavelengths, which indicates a spectral type somewhat cooler (A0) than the temperature we obtain from the Balmer jump. There is a slight chance that this is a composite spectrum; thus, this target is also not used for the determination of

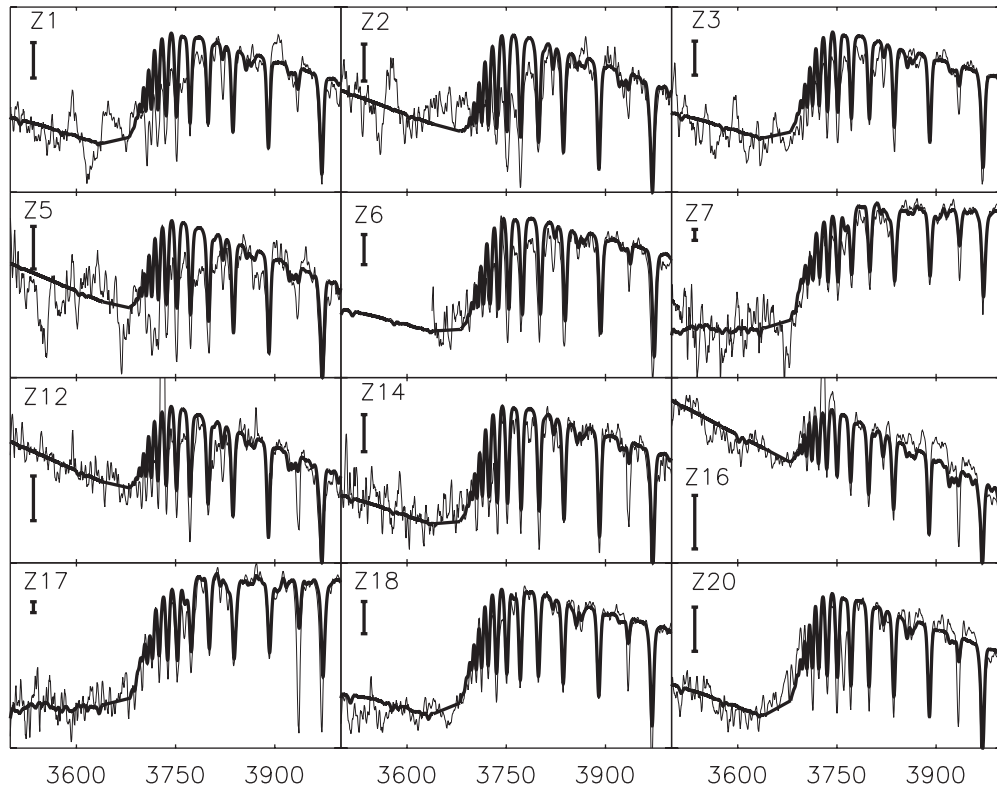


Figure 5. Balmer jump fit for 12 objects in field Z. Logarithm of flux is plotted vs. wavelength in Å. The bar in each panel indicates 0.05 dex changes in flux level.

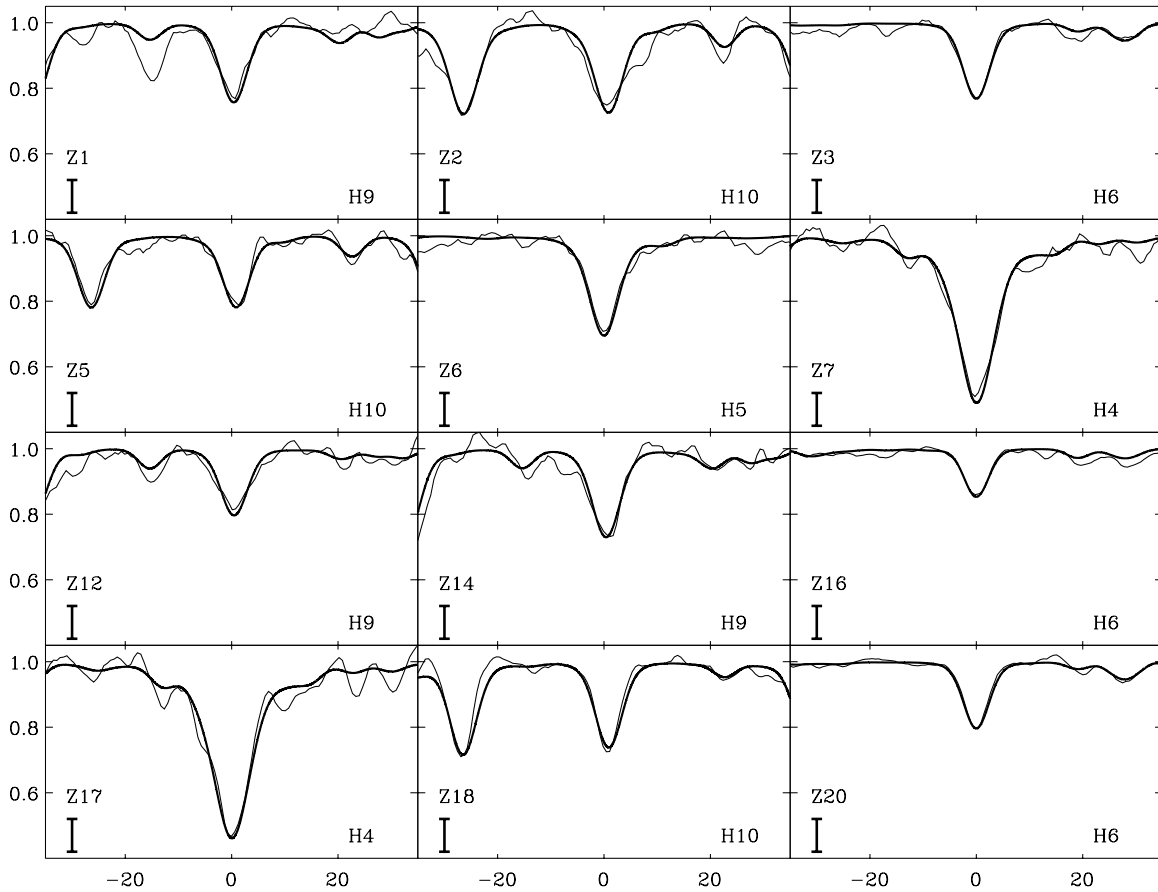


Figure 6. Balmer line fit for 12 objects in field Z. Normalized flux is plotted vs. wavelength displacement from the line center in Å.

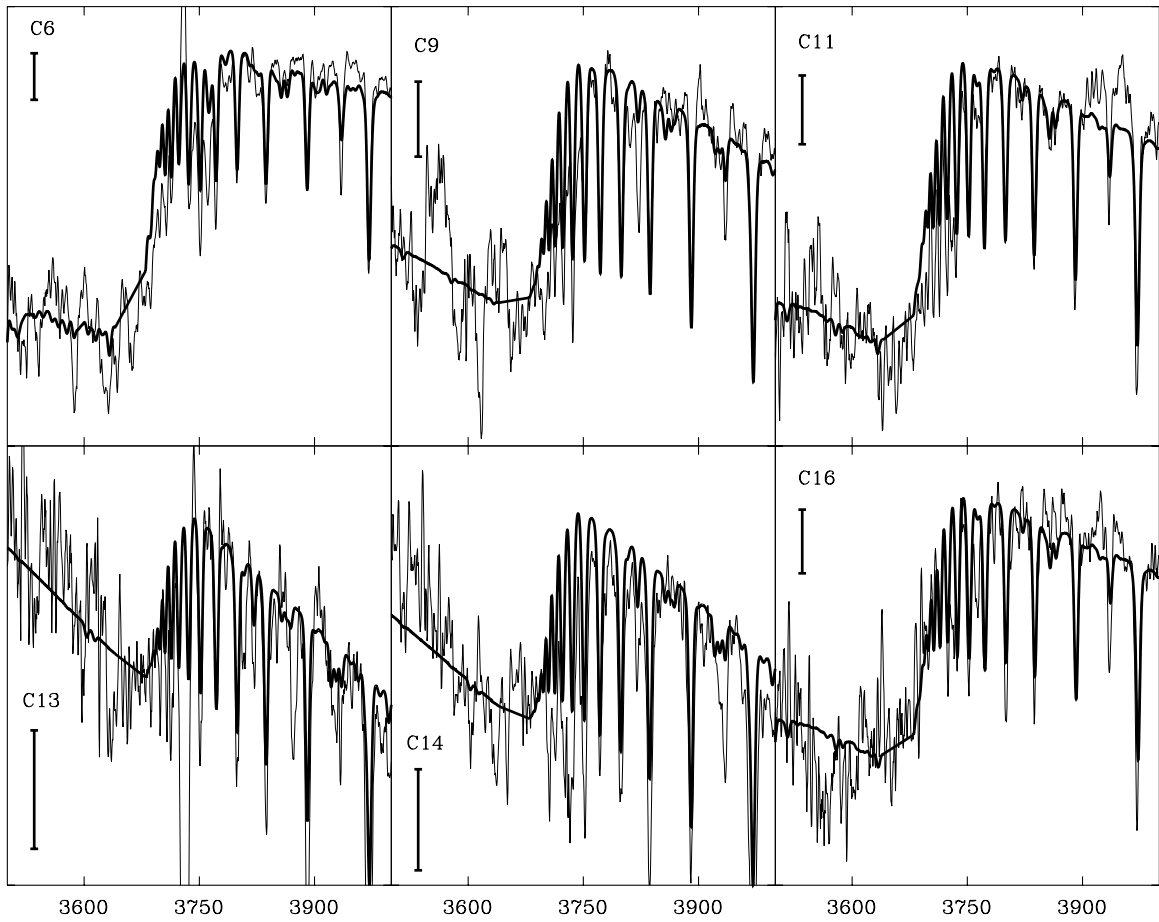


Figure 7. Balmer jump fit for six objects in field C. Logarithm of flux is plotted vs. wavelength in Å. The bar in each panel indicates 0.05 dex changes in flux level.

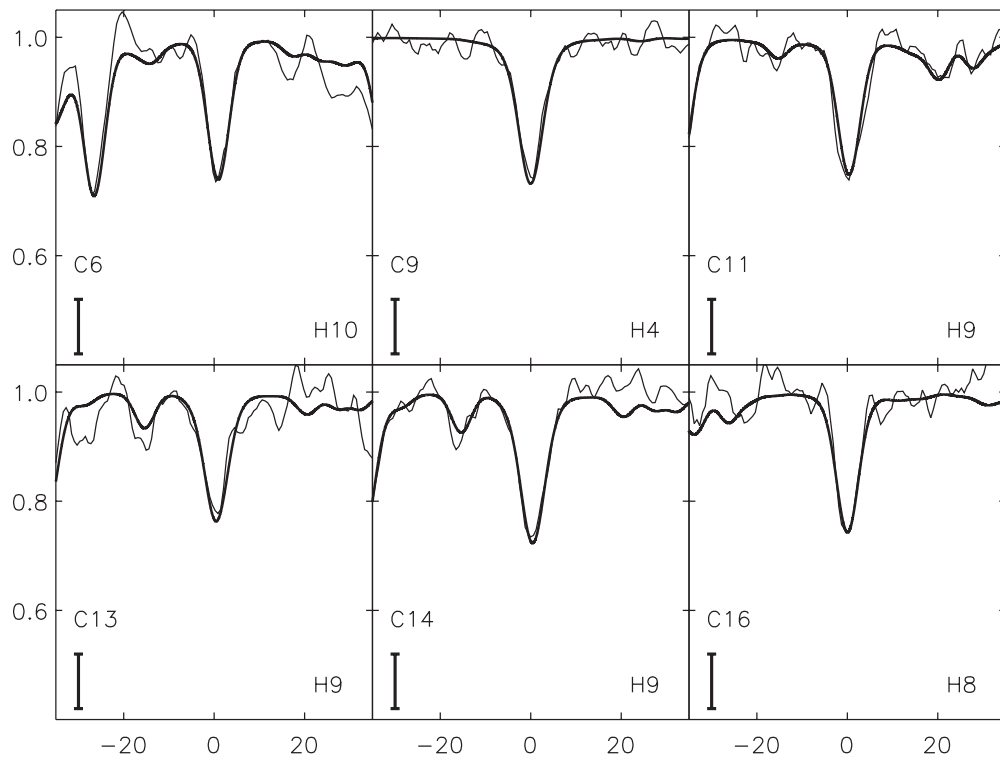


Figure 8. Balmer line fit for six objects in field C. Normalized flux is plotted vs. wavelength displacement from the line center in Å.

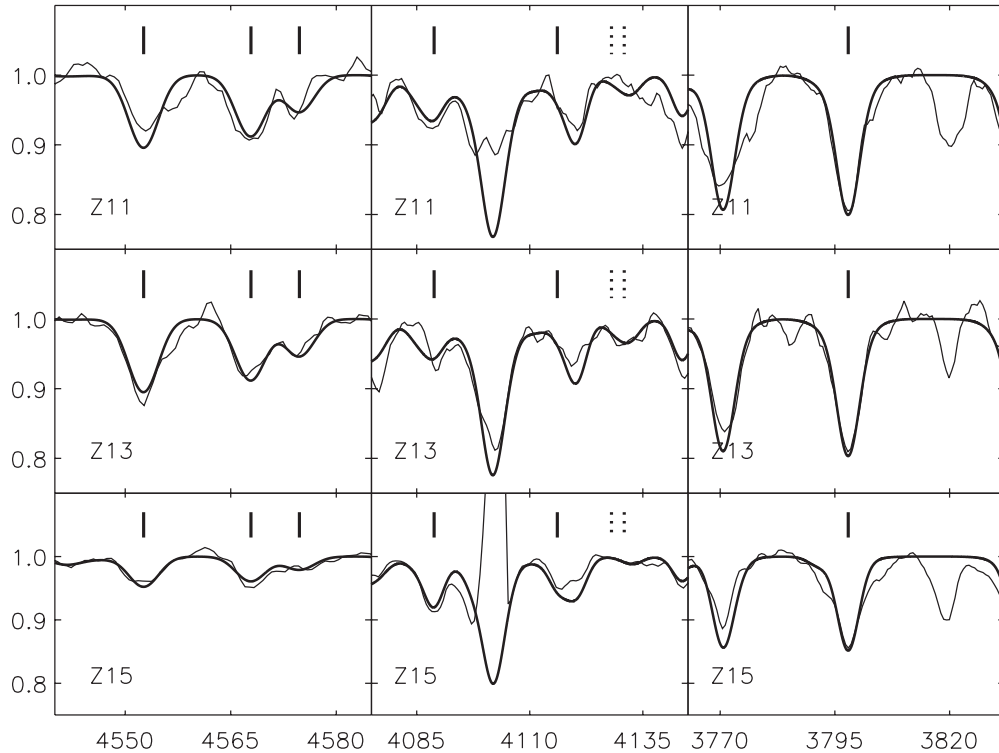


Figure 9. Si III line fits (left), Si IV (solid bars) and Si II (dotted bars) line fits (middle), and hydrogen H I line fits (right) for the three early B supergiants of our sample. Note that Si IV $\lambda 4116$ is blended by He I. Normalized flux is plotted vs. wavelength in Å.

metallicity (and also not for distance determination; see below). While this reduces the number of targets suitable for a metallicity determination, it still leaves us with a sub-sample of 15 objects large enough to constrain average metallicity and metallicity gradient of M81, as we will show below. For the measurement of metallicity we apply the technique developed by Kudritzki et al. (2008). For each star we identify spectral windows in the observed spectrum, which are free of strong Balmer lines, nebular emission lines, or spectral flaws caused by improper correction for cosmic-ray hits and for which the continuum of the normalized spectrum can be easily matched with the one of the synthetic spectra. A pixel-by-pixel comparison of observed and calculated normalized fluxes as a function of metallicity then allows for a calculation of $\chi^2([Z])$ in each spectral window i and the determination of $[Z]_i$ at which χ^2 is minimal. For this comparison, the observed spectra are renormalized for each metallicity so that the synthetic spectrum always intersects the observations at the same value at the edges of the spectral window (see also Kudritzki et al. 2008). An average of all $[Z]_i$ is then used as the measure of metallicity (for details, see again Kudritzki et al. 2008). An example is given in Figures 10 and 11 for target C20.

While the analysis method is straightforward and has been tested carefully in previous work, two obvious issues, unresolved binarity and blending with fainter sources in the galaxy studied, need to be discussed as possible sources of systematic uncertainties. Unresolved binarity can affect the analysis in two ways: first, through the contribution of a secondary to the photometric fluxes and the spectrum, and second, through the effects of close binary evolution with mass transfer or mass loss. In the first case, it is very unlikely that both components have a very similar spectral type and luminosity because of the very short lifetime in the supergiant stage. The most likely case is a secondary of lower mass still on the main sequence. However, such

an object would be much fainter by several magnitudes and not affect the spectroscopic analysis or the photometry. The second case is more serious but would affect only the FGLR-distance determination. Binary-induced mass transfer or mass loss would change the stellar mass at a given luminosity and create outliers from the FGLR relationship. Such outliers have been found by Kudritzki et al. (2008) and U et al. (2009). They are usually also outliers, when the mass–luminosity relationships of the targets are plotted. We will investigate the latter relationship in Section 5 (Figure 14).

Blending does not appear to be a problem because of the enormous optical brightness of the supergiants as already discussed in Kudritzki et al. (2008). The study by Bresolin et al. (2005) shows that at the distance of NGC 300 at 2 Mpc even ground-based photometry of BSGs is accurate and not affected by blending. Thus, at 3.5 Mpc for M81 with *HST* imaging and with our careful selection of targets (see Section 2) we do not expect blending effects influencing the photometry and, therefore, also not the spectroscopy. Of course, in individual cases there is always the very small chance of an unresolved coincidence of a target with another bright source. In such cases, the likelihood that the unresolved blends have the same spectral type is extremely small, again because of the short lifetime of BSGs. Thus, significant blends should be recognized in the spectrum. Target Z20 might be such a case. We also refer the reader to the careful modeling of blending effects in the *HST* imaging of Cepheids out to galaxies with 30 Mpc distances (Riess et al. 2009a, 2011), resulting in magnitude corrections of the order of only 0.1 mag. Cepheids are 3–6 mag fainter than BSGs. Thus, since Cepheids are only very weakly affected by blending, we do not expect significant effects for supergiants.

The results of the spectroscopic analysis are summarized in Table 2. Generally, the stellar parameters and their uncertainties

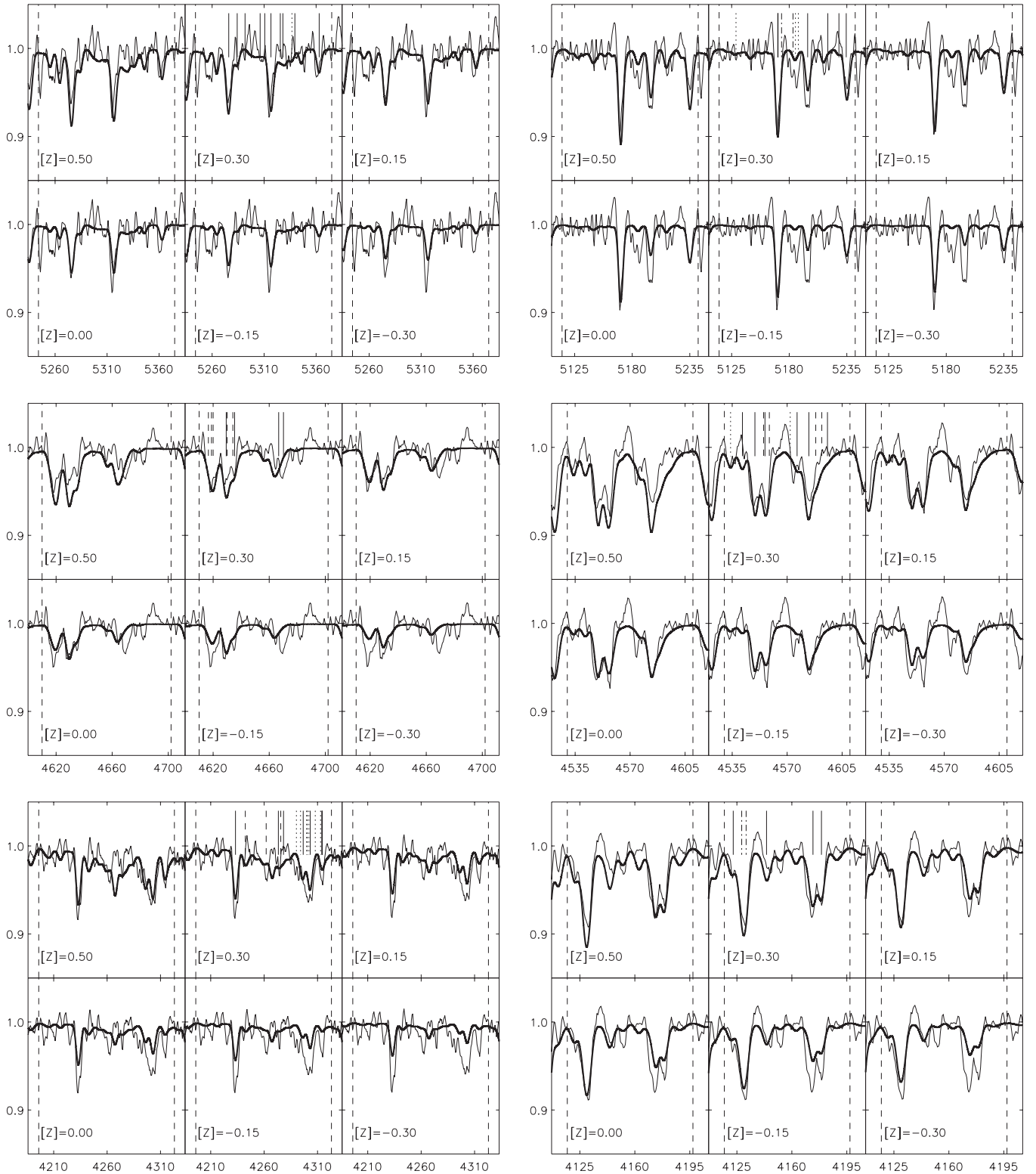


Figure 10. Metallicity fits in six spectral windows of object C20. The synthetic spectra are plotted in bold, and the metallicity is indicated at the left bottom of each plot. Normalized flux is plotted vs. wavelength in \AA . Fe lines are indicated by solid bars, Cr: dashed, Ti: dotted, Si: dash-dotted, Mg: dash-triple dotted. Only 6 of the 14 available metallicities are shown.

are comparable to those obtained in our previous work for galaxies less distant (see Kudritzki et al. 2008; Urbaneja et al. 2008). We conclude that for this type of low-resolution quantitative spectroscopy the step from 1 Mpc (WLM) over 2 Mpc (NGC 300) to now 4 Mpc is entirely feasible. In the following, we discuss the results in detail.

4. REDDENING AND EXTINCTION

As described above, one of the advantages of the spectroscopic analysis is that it provides information about interstellar reddening. For massive stars imbedded into the dusty disk of a star-forming spiral galaxy we expect a wide range of

Table 2
Stellar Parameters

No.	Name	T_{eff} (K)	$\log g$ (cgs)	$\log g_F$ (cgs)	[Z] (dex)	$E(B - V)$ (mag)	BC (mag)	m_{bol} (mag)	(10)
(1)	(2)	(3)	(4)	(5)	(6)	(7)	(8)	(9)	
0	Z1	12500 ⁹¹⁰ ₁₀₂₀	1.75 ^{0.17} _{0.20}	1.36 ^{0.05} _{0.06}	-0.07 ± 0.15	0.13	-0.75	19.78 \pm 0.18	
1	Z2	15000 ⁷³⁰ ₈₂₀	2.20 ^{0.13} _{0.15}	1.50 ^{0.05} _{0.05}	-0.01 ± 0.20	0.15	-1.15	19.88 \pm 0.16	
2	Z3	12500 ⁹⁶⁰ ₁₀₉₀	1.73 ^{0.18} _{0.21}	1.34 ^{0.05} _{0.06}	-0.09 ± 0.10	0.17	-0.75	19.56 \pm 0.19	
3	Z4	10000 ⁵⁰⁰ ₅₀₀	1.45 ^{0.17} _{0.18}	1.45 ^{0.08} _{0.09}		0.22	-0.28	19.36 \pm 0.13	a
4	Z5	16000 ⁸⁹⁰ ₁₀₂₀	2.15 ^{0.14} _{0.17}	1.33 ^{0.05} _{0.05}	0.03 ± 0.20	0.21	-1.29	19.54 \pm 0.17	b
5	Z6	12500 ⁶⁷⁰ ₆₈₀	1.95 ^{0.15} _{0.15}	1.56 ^{0.05} _{0.06}	0.08 ± 0.10	0.28	-0.73	19.61 \pm 0.15	
6	Z7	8500 ¹⁸⁰ ₁₃₀	1.40 ^{0.17} _{0.14}	1.68 ^{0.13} _{0.11}	-0.03 ± 0.20	0.23	0.02	20.76 \pm 0.10	
7	Z9	8300 ²⁰⁰ ₂₀₀	1.20 ^{0.19} _{0.24}	1.52 ^{0.15} _{0.20}		0.31	0.05	20.35 \pm 0.10	a
8	Z10	11000 ⁴⁴⁰ ₄₆₀	1.75 ^{0.13} _{0.14}	1.58 ^{0.06} _{0.07}	0.11 ± 0.10	0.25	-0.45	20.03 \pm 0.13	
9	Z11	22000 ¹⁰⁰⁰ ₁₀₀₀	2.62 ^{0.18} _{0.18}	1.25 ^{0.10} _{0.10}		0.24	-2.12	18.47 \pm 0.15	c
10	Z12	15000 ¹¹⁰⁰ ₁₄₂₀	1.95 ^{0.17} _{0.22}	1.25 ^{0.05} _{0.05}	0.07 ± 0.10	0.30	-1.17	18.92 \pm 0.20	
11	Z13	21000 ¹⁰⁰⁰ ₁₀₀₀	2.54 ^{0.18} _{0.18}	1.25 ^{0.10} _{0.10}		0.29	-2.01	18.19 \pm 0.16	c
12	Z14	13000 ⁷⁸⁰ ₈₇₀	1.90 ^{0.15} _{0.17}	1.44 ^{0.05} _{0.05}	0.21 ± 0.15	0.31	-0.83	19.59 \pm 0.17	
13	Z15	25000 ¹⁰⁰⁰ ₁₀₀₀	2.64	1.05		0.32	-2.45	17.04 \pm 0.17	c,d
14	Z16	15000 ¹⁰⁰⁰ ₁₀₀₀	1.80 ^{0.16} _{0.17}	1.10 ^{0.05} _{0.05}	0.09 ± 0.10	0.27	-1.29	18.08 \pm 0.17	b
15	Z17	8300 ¹²⁰ ₁₄₀	1.35 ^{0.14} _{0.18}	1.67 ^{0.12} _{0.15}	0.14 ± 0.15	0.34	0.05	20.13 \pm 0.10	
16	Z18	11500 ⁷⁷⁰ ₆₈₀	1.65 ^{0.17} _{0.17}	1.41 ^{0.06} _{0.06}	0.15 ± 0.10	0.27	-0.56	18.99 \pm 0.17	
17	Z20	12000 ¹¹⁶⁰ ₁₃₄₀	1.55 ^{0.23} _{0.27}	1.23 ^{0.05} _{0.05}		0.36	-0.69	18.51 \pm 0.23	e
18	C6	9250 ⁵⁶⁰ ₃₀₀	1.20 ^{0.21} _{0.14}	1.34 ^{0.11} _{0.09}	0.00 ± 0.10	0.28	-0.16	19.75 \pm 0.23	
19	C9	13000 ⁷⁸⁰ ₈₇₀	1.90 ^{0.15} _{0.17}	1.44 ^{0.05} _{0.05}		0.17	-0.83	19.86 \pm 0.17	
20	C11	11000 ⁶⁷⁰ ₇₂₀	1.55 ^{0.17} _{0.19}	1.38 ^{0.06} _{0.07}	0.04 ± 0.15	0.34	-0.47	18.88 \pm 0.15	
21	C13	17000 ⁸³⁰ ₉₆₀	2.27 ^{0.13} _{0.15}	1.35 ^{0.05} _{0.05}		0.19	-1.49	19.09 \pm 0.16	b
22	C14	17000 ⁷⁰⁰ ₇₉₀	2.37 ^{0.12} _{0.13}	1.45 ^{0.05} _{0.05}		0.19	-1.49	19.33 \pm 0.15	b
23	C16	11000 ⁶⁷⁰ ₇₂₀	1.55 ^{0.17} _{0.19}	1.38 ^{0.06} _{0.07}		0.38	-0.47	19.58 \pm 0.15	
24	C20	10500 ⁴⁷⁰ ₅₂₀	1.60 ^{0.15} _{0.17}	1.52 ^{0.07} _{0.08}	0.12 ± 0.10	0.30	-0.36	19.12 \pm 0.15	
25	C21	12500 ⁵⁰⁰ ₅₀₀	1.75 ^{0.12} _{0.12}	1.36 ^{0.05} _{0.05}		0.19	-0.75	19.07 \pm 0.13	a

Notes.

^a No D_B , T_{eff} from spectral type; not used for distance determination.

^b T_{eff} from D_B and Si II, Si III, Si IV.

^c T_{eff} from Si II, Si III, Si IV.

^d Extreme H II contamination of Balmer lines; not used for distance determination.

^e T_{eff} hotter than indicated by spectral type; not used for distance determination.

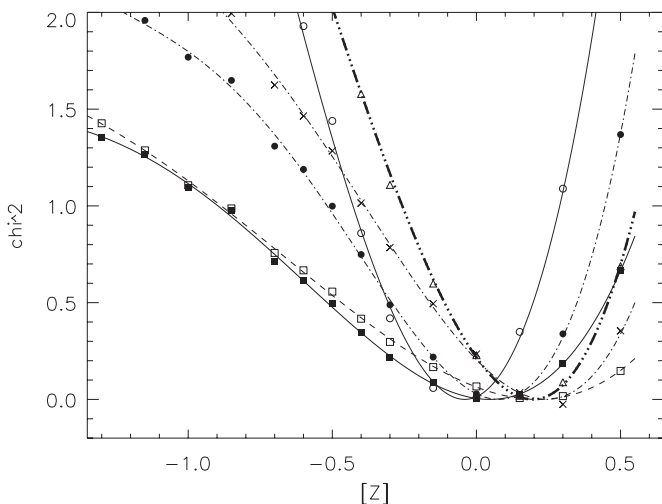


Figure 11. $\chi^2([Z])$ for each spectral window of object C20 as a function of metallicity $[Z]$. The curve for each window has a well-defined minimum abscissa $[Z]_i$. The average of all $[Z]_i$ is adopted as the stellar metallicity value.

interstellar reddening. Indeed, we find a range from $E(B - V) = 0.13$ to 0.38 mag. Figure 12 shows the distribution of interstellar reddening among our targets. The average value is $E(B - V)_{\text{av}} = 0.26$ mag. The foreground reddening is 0.08 mag (Schlegel et al. 1998). Our reddening values include both intrinsic and foreground reddening. We stress that our average value of $E(B - V)$ may underestimate the average reddening in M81, as our target selection (see Figure 1) is biased toward lower reddening.

Figure 12 shows reddening as a function of galactocentric distance. While the scatter is large, it is still tempting to fit a regression to the data. We find

$$E(B - V) = (0.415 \pm 0.025) - (0.0243 \pm 0.0037) \times d/\text{kpc}. \quad (2)$$

The lower reddening beyond 10 kpc indicated by this regression is in agreement with the results found by Williams et al. (2009), who investigated star formation history and metallicity with *HST* CMDs in the outer fields of M81 and found $E(B - V) = 0.14$ mag at 14 kpc galactocentric distance.

We note that the reddening values found in our study are much larger than the value of 0.03 mag originally assumed in the *HST*

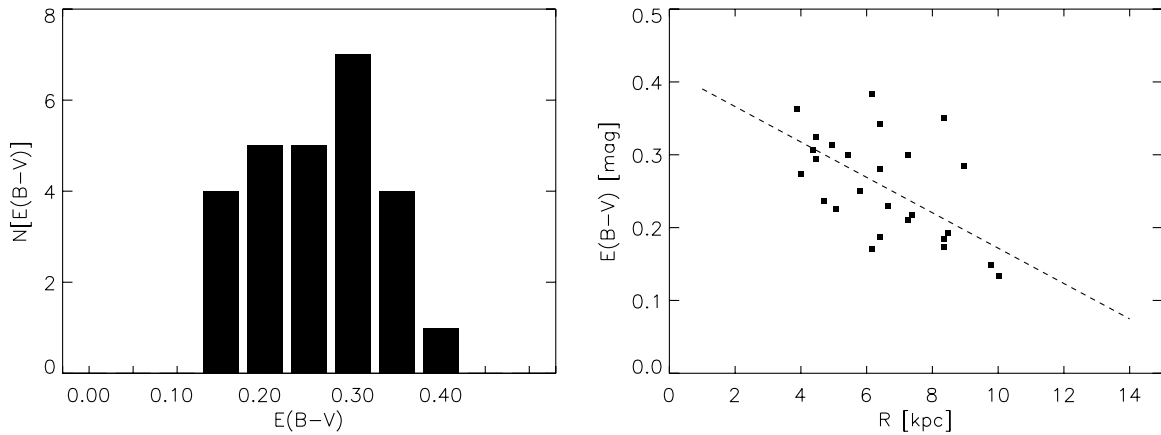


Figure 12. Interstellar reddening in M81. Left: histogram of the $E(B - V)$ distribution. Right: $E(B - V)$ as a function of galactocentric distance with the regression curve (dashed) discussed in the text.

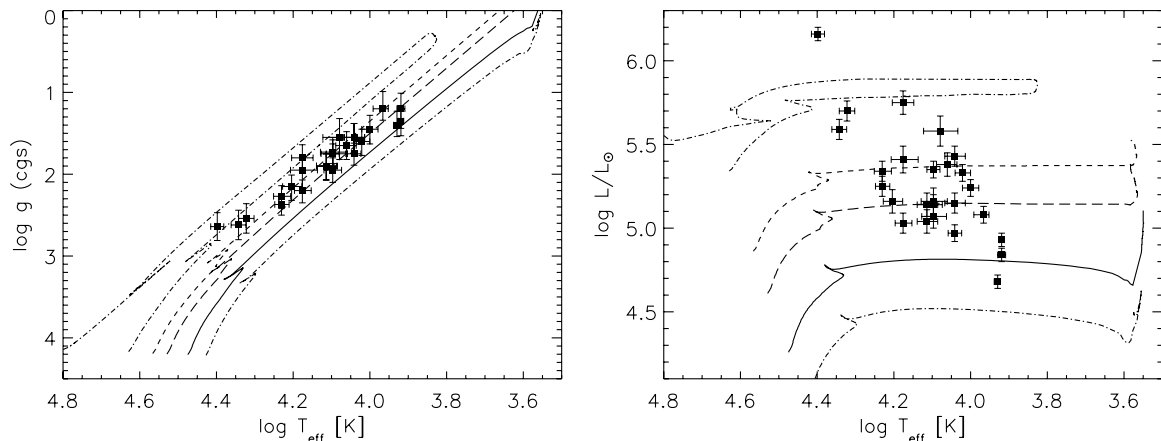


Figure 13. Stellar parameters of the observed sample of M81 supergiants compared with evolutionary tracks for the Milky Way metallicity including the effects of rotational mixing (Meynet & Maeder 2003). Left: $(\log g, \log T_{\text{eff}})$ -diagram. Right: H-R diagram. The zero-age main-sequence masses are (in increasing luminosity/decreasing gravity) 12, 15, 20, 25, 40 solar masses, respectively.

distance scale Key Project (Freedman et al. 1994) for Cepheids at inner fields between 3 and 6 kpc galactocentric distance. The final Key Project study (Freedman et al. 2001) obtained an average value of $E(B - V) = 0.15$ mag, still significantly smaller than our value, in particular in view of the fact that a difference of 0.1 mag in reddening results in a difference of 0.3 mag in distance modulus if the ratio of total to selective extinction is $R_V = 3.1$.

5. STELLAR PROPERTIES AND EVOLUTION

Figure 13 (left panel) shows the location of all targets in the $(\log g, \log T_{\text{eff}})$ -plane compared with evolutionary tracks (Meynet & Maeder 2003), which were calculated for solar metallicity and include the effects of rotational mixing and anisotropic mass loss. The advantage of a diagram of this type is that it is independent of any assumption on distance and relies completely on the results of the spectroscopic analysis (on the other hand, systematic effects in the evolutionary tracks might affect the comparison). The targets form an evolutionary sequence crossing from the main sequence toward the red supergiant stage with initial zero-age main-sequence (ZAMS) masses between 15 and $50 M_{\odot}$ and the majority of objects with ZAMS masses about $20\text{--}25 M_{\odot}$.

A complementary way to discuss stellar evolution and stellar properties is the HRD. This requires information about the distance. In Section 8, we will use the FGLR to determine

a distance modulus of $\mu = 27.7 \pm 0.1$. With this distance and using the spectroscopically determined reddening and extinction and the bolometric corrections provided by the model atmospheres for the final parameters of temperature, gravity, and metallicity we can determine absolute bolometric magnitudes, luminosities, and stellar radii. In the calculation of stellar radii from luminosities we take into account that the errors in luminosity are dominated by the errors in effective temperature and are, thus, correlated (maximum luminosity corresponds to maximum temperature and, thus, minimum radius, whereas minimum luminosity at minimum temperature yields maximum radius). The results are given in Table 3, and the resulting HRD is shown in Figure 13 (right panel).

The HRD confirms that the majority of targets are in the ZAMS mass range of about $20\text{--}25 M_{\odot}$ and are generally consistent with the $(\log g, \log T_{\text{eff}})$ -diagram. However, one object (Z15) sticks out as very luminous. We recall that the spectroscopic analysis of this object was difficult because of extremely strong contamination with nebular H II emission, which might affect the determination of gravity in a systematic way that is difficult to assess. In consequence, we have not included this object in the FGLR determination of the distance.

With the stellar radii determined from the luminosities we can use the gravities to estimate spectroscopic stellar masses. Those are also given in Table 3. An alternative way to estimate masses is to use stellar luminosities and to compare with the luminosities

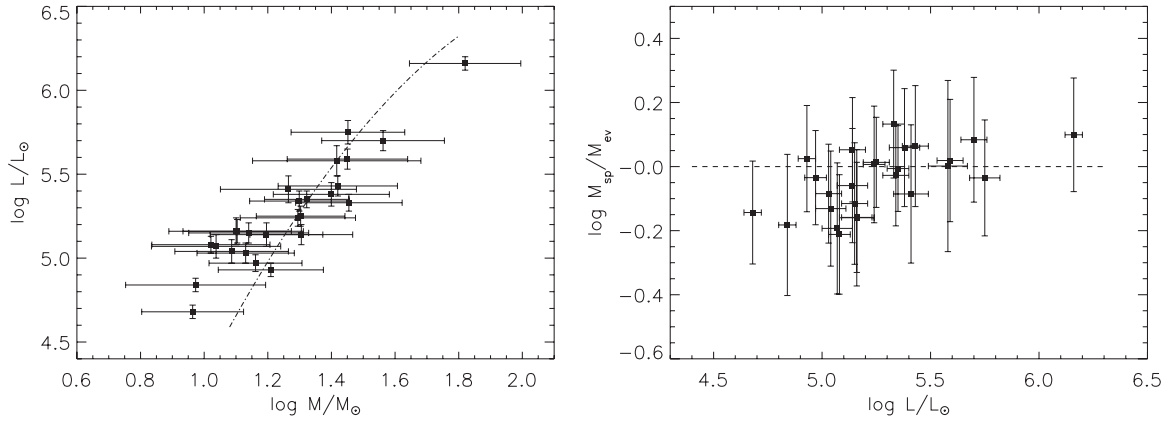


Figure 14. Left: observed mass–luminosity relationship compared with stellar evolution theory using the tracks from Figure 13 at an effective temperature of 10^4 K. Right: logarithmic ratio of spectroscopic to evolutionary masses as a function of luminosity.

Table 3
Absolute Magnitudes, Luminosities, Radii, and Masses

No.	Name	M_V (mag)	M_{bol} (mag)	$\log L/L_{\odot}$ (dex)	R (R_{\odot})	M_{spec} (M_{\odot})	M_{evol} (M_{\odot})
(1)	(2)	(3)	(4)	(5)	(6)	(7)	(8)
0	Z1	−7.16	−7.92	5.07 ± 0.07	73.1 ± 6.2	10.9	17.0
1	Z2	−6.67	−7.82	5.03 ± 0.06	48.5 ± 3.5	13.5	16.4
2	Z3	−7.38	−8.14	5.16 ± 0.08	80.9 ± 7.1	12.6	18.2
3	Z4	−8.08	−8.34	5.24 ± 0.05	138.6 ± 8.4	19.7	18.2
4	Z5	−6.90	−8.16	5.16 ± 0.07	49.8 ± 3.9	12.7	18.3
5	Z6	−7.36	−8.09	5.14 ± 0.06	79.1 ± 5.6	20.2	17.9
6	Z7	−6.96	−6.94	4.68 ± 0.04	100.7 ± 4.9	9.2	12.8
7	Z9	−7.37	−7.35	4.84 ± 0.04	127.6 ± 6.1	9.4	14.3
8	Z10	−7.24	−7.67	4.97 ± 0.05	84.2 ± 4.9	14.5	15.7
9	Z11	−7.12	−9.23	5.59 ± 0.06	43.2 ± 3.0	28.2	27.0
10	Z11	−7.61	−8.78	5.41 ± 0.08	75.5 ± 6.9	18.4	22.4
11	Z13	−7.49	−9.51	5.70 ± 0.06	53.9 ± 3.9	36.5	30.1
12	Z14	−7.29	−8.11	5.14 ± 0.07	73.8 ± 3.9	15.7	18.0
13	Z15	−8.20	−10.66	6.16 ± 0.04	64.6 ± 3.3	66.1	52.6
14	Z16	−8.56	−9.62	5.75 ± 0.07	111.1 ± 8.6	28.3	30.7
15	Z17	−7.59	−7.57	4.93 ± 0.04	141.2 ± 6.6	16.2	15.3
16	Z18	−8.14	−8.71	5.38 ± 0.07	124.3 ± 9.6	25.1	21.9
17	Z20	−8.49	−9.19	5.58 ± 0.09	142.4 ± 15.3	26.1	26.0
18	C6	−7.78	−7.95	5.08 ± 0.05	135.4 ± 8.4	10.5	17.1
19	C9	−7.01	−7.84	5.04 ± 0.07	65.2 ± 5.0	12.2	16.5
20	C11	−8.34	−8.82	5.43 ± 0.06	142.9 ± 10.1	26.3	22.7
21	C13	−7.14	−8.61	5.34 ± 0.06	54.3 ± 4.0	19.9	21.2
22	C14	−6.88	−8.37	5.25 ± 0.06	48.6 ± 3.3	20.1	19.5
23	C16	−7.63	−8.12	5.15 ± 0.06	103.5 ± 7.3	13.8	18.0
24	C20	−8.22	−8.58	5.33 ± 0.05	140.4 ± 8.4	28.5	21.0
25	C21	−7.89	−8.63	5.35 ± 0.05	101.4 ± 6.0	21.0	21.3

and actual masses at the BSG temperatures of evolutionary tracks. Evolutionary masses are also given in Table 3. They are determined from the BSG mass–metallicity relationship given by Kudritzki et al. (2008) (for Milky Way metallicity and including the effects of rotational mixing). We emphasize that both spectroscopic and evolutionary masses are present-day masses and are generally expected to be lower than the initial ZAMS masses through the effects of mass loss. Since the early work by Herrero et al. (1992), it has been found that spectroscopic masses are often significantly smaller than evolutionary masses, although with the development of fully line-blanketed model atmospheres and improved NLTE line formation the effect has become much smaller (see Kudritzki & Urbaneja 2009 for a review, and references therein). In

Figure 14, we check our sample for this effect by comparing the observed spectroscopic mass–luminosity relationship with the prediction of stellar evolution and by directly plotting the ratio of spectroscopic to evolutionary mass as a function of luminosity. We find a small effect only at the lower mass end, where spectroscopic masses appear to be somewhat smaller than evolutionary masses. However, we conclude that our sample is not significantly different from the one studied by Kudritzki et al. (2008) in NGC 300 and U et al. (2009) in M33.

6. METALLICITY, METALLICITY GRADIENT, AND CHEMICAL EVOLUTION

Metallicities of 15 targets together with their galactocentric distance are given in Table 2. This allows us to discuss stellar metallicity and the metallicity gradient in M81. Figure 15 (upper left panel) shows a plot of logarithmic metallicity relative to the Sun $[Z]$ as a function of galactocentric distance (at the distance of 3.47 Mpc; see Section 8; $R_{25} = 11.99$ arcmin corresponds to 12.09 kpc). A metallicity gradient of the young disk population in M81 is clearly visible. A linear regression (using the routine fitxy, Numerical Recipes; Press et al. 1992) yields

$$[Z] = (0.286 \pm 0.061) - (0.033 \pm 0.009) R/\text{kpc}. \quad (3)$$

With respect to the distance-independent-normalized angular galactocentric distance R/R_{25} we obtain

$$[Z] = (0.286 \pm 0.061) - (0.411 \pm 0.109) R/R_{25}. \quad (4)$$

As is evident from the plot and the regression, young massive stars in the disk of M81 have slightly supersolar metallicities at the inner regions and slightly subsolar metallicity in outer parts. The gradient is very shallow, though, compared with the less massive galaxies studied in our BSG project. For NGC 300 and M33 metallicity gradients were determined of 0.08 and 0.07 dex kpc^{-1} , respectively, by Kudritzki et al. (2008) and U et al. (2009). On the other hand, for the Milky Way, which has a mass comparable to M81, Daflon & Cunha (2004) in their spectroscopy of massive stars obtain a gradient of -0.031 ± 0.012 dex kpc^{-1} , very similar to our result. (We note, however, the results by Rolleston et al. 2000 for B stars and Luck et al. 2006, 2011 for Cepheids, who obtained 0.07 dex kpc^{-1} and 0.055 dex kpc^{-1} , respectively.)

Garnett & Shields (1987) and Stauffer & Bothun (1984) have analyzed H II region emission line spectra of M81 to derive

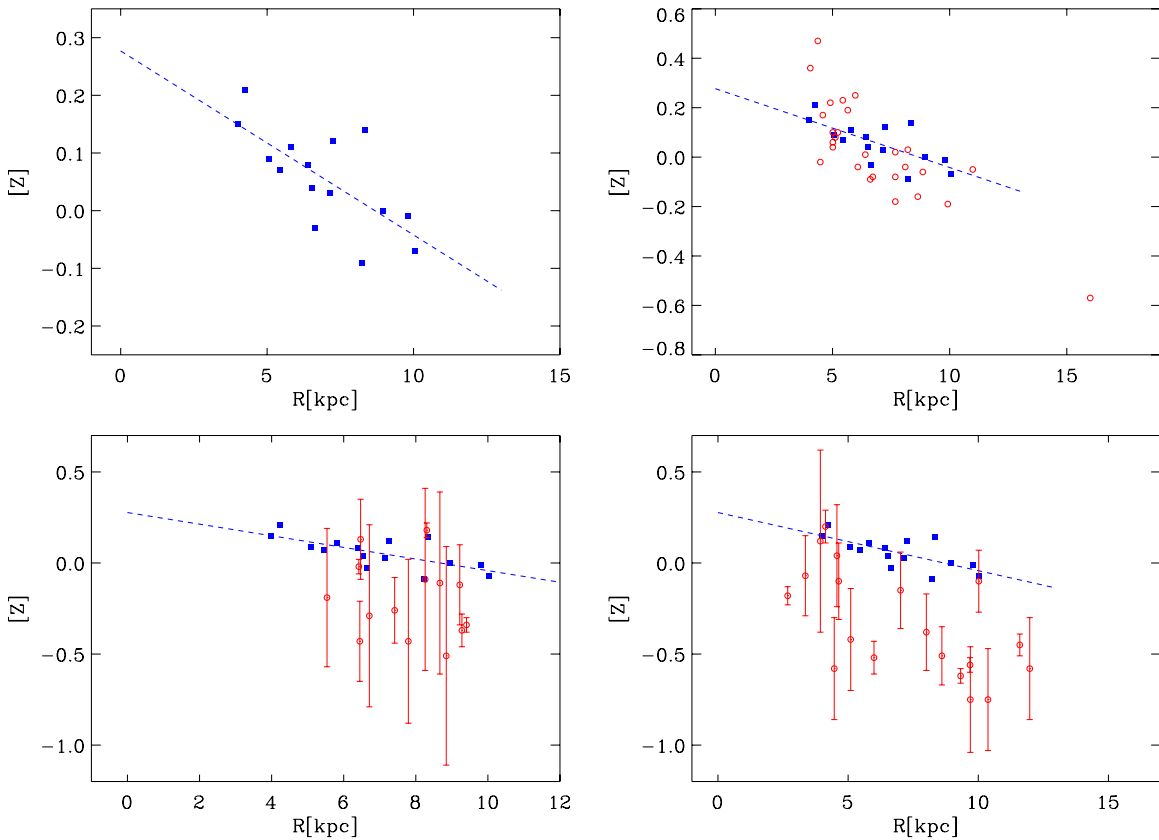


Figure 15. Upper left: metallicity of BSGs in M81 as a function of galactocentric distance in kpc. The dashed curve is the regression discussed in the text. Uncertainties are given in Table 2 and not plotted. Upper right: same as upper left, but with the oxygen abundances of H II regions from the strong-line studies by Garnett & Shields (1987) and Stauffer & Bothun (1984) overplotted. Random uncertainties of the H II region data are between 0.1 and 0.2 dex; systematic uncertainties are discussed in the text. Lower left: same as upper left, but with the H II region oxygen abundances by Stanghellini et al. (2010) overplotted. Lower right: same as upper left, but with oxygen abundances of PNe obtained by Stanghellini et al. (2010) overplotted with error bars. The dashed line in all four panels is the BSG regression obtained in this work. For a detailed discussion, see the text.

(A color version of this figure is available in the online journal.)

oxygen abundances as a function of galactocentric radius. They used a strong-line method following the calibration by Pagel et al. (1979) (Garnett & Shields 1987 also used photoionization models for an independent check of the abundances obtained). In Figure 15 (right upper panel), we overplot these results with the galactocentric distances corrected to the distance used in our work. In the range of 5–11 kpc there are a large number of objects in a similar abundance range as the BSGs with a slight offset of -0.1 dex. However, at 5 kpc and below there are several objects with very high oxygen abundance. This result might be an artifact of the strong-line calibration used. These inner data points together with the H II region Muench 1 at 16 kpc (carefully discussed in Garnett & Shields 1987) lead to an oxygen abundance gradient of -0.064 ± 0.020 dex kpc^{-1} with a significantly higher value of $[\text{O}] = 0.46 \pm 0.14$ dex at the center, where $[\text{O}]$ is defined in the same way as $[Z]$, namely, $[\text{O}] \equiv \log(\text{O}/\text{O}_{\odot}) = [\text{O}/\text{H}] - [\text{O}/\text{H}]_{\odot}$ with $[\text{O}/\text{H}] = 12 + \log(\text{O}/\text{H})$ and $[\text{O}/\text{H}]_{\odot} = 8.69$ dex (Allende Prieto et al. 2001).

The H II regions of M81 have also been included in the work by Zaritsky et al. (1994), who developed a different strong-line calibration method. Their central metallicity is even higher, $[\text{O}] = 0.51 \pm 0.11$ dex, and the gradient is 0.042 ± 0.015 dex kpc^{-1} , somewhat higher than the result of our BSG work. As has already been shown by Bresolin et al. (2009) and Bresolin (2011), this calibration leads to metallicities, which are too high when compared with H II region oxygen abundances based on electron temperature determinations with auroral lines

(see also Kudritzki et al. 2008 for a comparison with BSG metallicities). Our results support this conclusion.

Henry & Howard (1995) used published emission line fluxes of M81 and a series of photoionization models for a study of the oxygen abundance gradient. Their results yield a central value of $[\text{O}] = 0.26$ and a gradient of -0.074 dex kpc^{-1} (R. B. C. Henry 2011, private communication). The central value agrees with our BSG work, but the gradient is steeper.

Stanghellini et al. (2010) have recently studied PNe and H II regions in M81 and used the detection of auroral lines to determine nebular electron temperatures and abundances. Since according to Bresolin et al. (2009) this approach leads to more reliable results, a comparison with the Stanghellini et al. (2010) H II region oxygen abundances is important. This is done in Figure 15 (lower left panel). At first glance, there seem to be two groups of H II regions, one group with abundances comparable to the BSGs and another with abundances 0.4 dex smaller. However, for many of the objects the abundances are too uncertain with individual errors as large as up to 0.6 dex estimated by Stanghellini et al. (2010); thus, no clear conclusions are possible with regard to abundance and abundance gradient from this sample. Stanghellini et al. (2010) combine their sample with the one by Garnett & Shields (1987) to discuss metallicity and metallicity gradient. However, while the random errors of the Garnett & Shields (1987) sample are small (0.1–0.2 dex), the abundances are affected by the systematic uncertainties of the strong-line method. On the other

hand, for the Stanghellini et al. (2010) abundances the situation is opposite: the random errors are large and the systematic errors are strongly reduced. Thus, we think the combination of the two samples is subject to uncertainties that are difficult to estimate.

Contrary to their H II region observations, the PNe analyzed by Stanghellini et al. (2010) have abundances generally more accurate. In Figure 15 (lower right panel) they are also compared with the BSG metallicities. The average difference in metallicity between the PNe and the BSGs is about -0.4 dex and seems to be significant. The metallicity gradient is -0.057 ± 0.007 dex kpc^{-1} and steeper than for the BSGs. This is a very interesting result, since the PNe of this sample do not contain type I PN objects and consist only of types II and III, which means that they are significantly older than the BSGs with average ages of 3 and 6 Gyr, respectively (Maciel et al. 2010; Stanghellini & Haywood 2010). This means that over the last 5 Gyr the metallicity must have increased substantially and the metallicity gradient of the disk has become shallower.

Photometric investigations of the disk of M81 confirm this conclusion. Williams et al. (2009) in their comprehensive study of star formation and metallicity analyzing *HST* CMDs of an outer disk field at $R/R_{25} = 1.17$ find metallicities in the range between $[Z] = -0.6$ and -0.3 dex, for the population with ages between 10 Gyr and 50 Myr. They also find solar metallicity for the younger population. This result is in agreement with Tikhonov et al. (2005), who investigated *HST* CMDs of a different disk field, and Davidge (2009), who used the red giant branch from CFHT MegaCam CMDs over the whole disk of M81 to also estimate a metallicity of $[Z] = -0.4$ dex. While metallicities obtained in this way might suffer from uncertainties in the extinction adopted and the systematics of the isochrones used, the picture emerging from the combination of our BSG results, the PNe observed, and CMDs studied indicates that for a long period the metallicity of the M81 disk remained roughly constant and subsolar, but obviously, before the birth of the young population of massive stars, there must have been a phase of enrichment.

This situation is different from the Milky Way. Young massive stars have a metallicity very similar to the Sun (Przybilla et al. 2008b). PN metallicities are also very close to the one of the Sun and to massive stars (Henry et al. 2010; Stanghellini & Haywood 2010). The metallicity enrichment of the thin disk has been very slow with an estimated increase of metallicity $\Delta[Z] = 0.017$ dex Gyr^{-1} , and the metal-poor ($[Z] - 0.58$ dex) thick disk may have formed 12–13 Gyr ago in a single starburst (Fuhrmann 2011). We also note that the case of M33 is similar to the Milky Way (Bresolin et al. 2010; Urbaneja et al. 2005b). At this point, one can only speculate what caused the late enrichment of the very young population in M81. An interesting thought has been formulated by Williams et al. (2009). M81 has satellite galaxies such as NGC 3077 and M82, which are gas and metal rich (Martin 1997) and are involved in tidal interaction with M81 (Appleton et al. 1981; Heckman et al. 1990). Recent inflow from such satellites or the tidal interaction induced by them and leading to recent bursts of star formation could then have influenced the chemical evolution.

Chemical evolution models of galaxies also predict changes of the metallicity gradients as a function of time, however, many times with qualitatively different results. For instance, Chiappini et al. (2001) predict gradients to become steeper with time, whereas Hou et al. (2000) predict the opposite. Simulations of disk evolution including the effects of stellar migration by Roškar et al. (2008) also predict a flattening of the gradient

through the homogenization of the population in the disk as a function of time.

The comparison of PNe with a younger stellar generation such as massive stars or H II regions offers, in principle, an opportunity to provide observational constraints. In the case of the Milky Way Stanghellini & Haywood (2010) conclude that the gradient is steepening with time. However, Maciel & Costa (2009) find the opposite, whereas Henry et al. (2010) do not find any hints of evolution at all. Thus, the situation of the temporary evolution of the Milky Way abundance gradient remains controversial. In M81 comparing our BSG results with the PN abundances determined by Stanghellini et al. (2010), we find a weak indication that the abundance gradient became shallower with time.

7. MASS–METALLICITY RELATIONSHIP OF GALAXIES FROM BSG SPECTROSCOPY

Since the early work by Lequeux et al. (1979) the mass–metallicity relationship of star-forming galaxies has been regarded as an important observational constraint for understanding galaxy formation and evolution (see references introduced in the discussion). While these pioneering investigations were restricted to a relatively small sample of galaxies, the recent spectroscopic surveys such as SDSS opened the opportunity to study a large number of such objects. Tremonti et al. (2004) have analyzed more than 50,000 galaxies observed within SDSS and obtained a well-defined relationship between oxygen abundance and total stellar mass. However, the oxygen abundances are again based on the use of strong H II region emission lines only. While Tremonti et al. (2004) took special care of this problem and developed their own calibration of their strong-line method, the systematic uncertainties are important to be investigated. Bresolin et al. (2009) found that this calibration very likely overestimates oxygen abundances. In a more general approach, Kewley & Ellison (2008) demonstrated very clearly that the mass–metallicity relationship obtained from the standard strong lines of H II regions depends very strongly on the calibration of the strong-line method used. Applying 10 different calibrations, which are frequently used in H II region abundance studies, on the same data set of emission lines of about 20,000 SDSS galaxies, Kewley & Ellison (2008) obtained the shocking result that the mass–metallicity relationship can change from steep to almost flat just dependent on the calibration used. Since all the work published with regard to this relationship seems to rely on strong-line H II region data, and given these systematic uncertainties, it seems appropriate to start an investigation based on stellar spectroscopy only. With the results obtained here and compiling the metallicities of the BSG quantitative spectroscopy work for other galaxies published so far we have made a first attempt.

The compilation of galaxy masses and metallicities is given in Table 4. For the spiral galaxies with a clear metallicity gradient (NGC 300, M33, MW, M31, M81) metallicity values were taken at galactocentric distances of two disk scale lengths. For the irregular Local Group galaxies average values were used. The data are plotted in Figure 16 (left panel). A very clear correlation of metallicity with stellar mass is obtained.

While the weakness of our approach at this stage is the small size of our sample, it is tempting to compare with the SDSS H II region based results discussed. For this purpose we have overplotted the average mass–metallicity relationships obtained by Kewley & Ellison (2008) for the 10 different calibrations

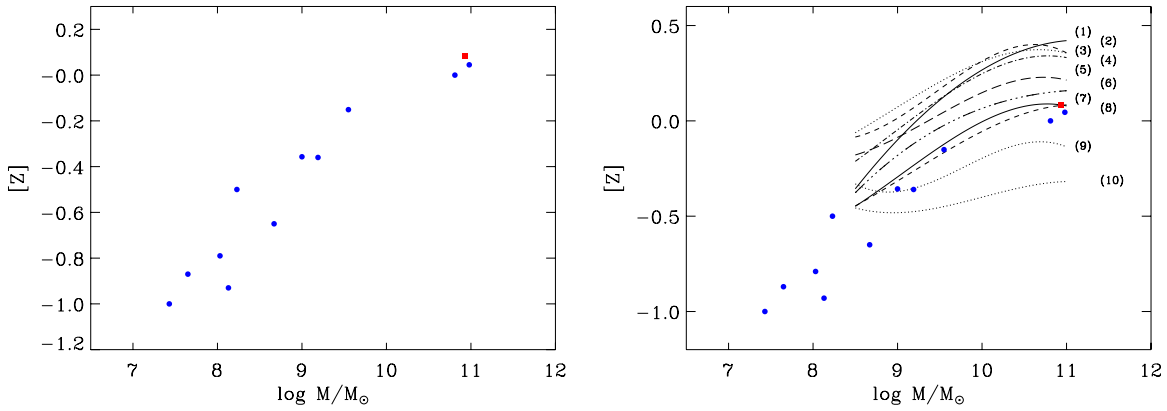


Figure 16. Left: observed mass–metallicity relationship of galaxies obtained from spectroscopic studies of BSGs. The red square is the M81 result from this paper. Right: same as left, but now with the average relationships obtained by Kewley & Ellison (2008) for the 10 different H II region strong-line calibrations used in their study of 20,000 SDSS galaxies. The 10 calibrations are (1) solid, Tremonti et al. (2004); (2) dashed, Zaritsky et al. (1994); (3) dotted, Kobulnicky & Kewley (2004); (4) dash-dotted, Kewley & Dopita (2002); (5) long-dashed, McGaugh (1991); (6) dash-triple-dotted, Denicoló et al. (2002); (7) solid, Pettini & Pagel (2004) (using [O III]/H β and [N II]/H α); (8) dashed, Pettini & Pagel (2004) (using [N II]/H α); (9) dotted, Pilyugin (2001); (10) dotted, Pilyugin & Thuan (2005). (A color version of this figure is available in the online journal.)

Table 4
Mass–Metallicity Relationship of Galaxies

Galaxy	$\log M_{\text{stars}}/M_{\odot}$	[Z]	Source	Source
(1)	(2)	(dex)	(mass)	[Z]
		(3)	(4)	(5)
M81	10.93	0.08	a	b
M31	10.98	0.04	c	d,e,f
MW	10.81	0.00	g	h
M33	9.55	−0.15	i	j
NGC 300	9.00	−0.36	k	l
LMC	9.19	−0.36	i	m
SMC	8.67	−0.65	i	n,o
NGC 6822	8.23	−0.50	i	p
NGC 3109	8.13	−0.93	i	q
IC1613	8.03	−0.79	i	r
WLM	7.67	−0.87	i	s
Sex A	7.43	−1.00	i	t

Notes.

- ^a de Blok et al. (2008).
- ^b This work.
- ^c Chemin et al. (2009).
- ^d Przybilla et al. (2008a).
- ^e Trundle et al. (2002).
- ^f Smartt et al. (2001).
- ^g Sofue et al. (2009).
- ^h Przybilla et al. (2008b).
- ⁱ Woo et al. (2008).
- ^j U et al. (2009).
- ^k Kent (1987).
- ^l Kudritzki et al. (2008).
- ^m Hunter et al. (2007).
- ⁿ Schiller (2010).
- ^o Trundle & Lennon (2005).
- ^p Venn et al. (2001).
- ^q Evans et al. (2007).
- ^r Bresolin et al. (2007).
- ^s Urbaneja et al. (2008).
- ^t Kaufer et al. (2004).

used in their work. It seems that a few of these calibrations (Tremonti et al. 2004; Zaritsky et al. 1994) lead to a much steeper relationship than our work, whereas others (Pettini & Pagel 2004) are in much better agreement. We note that our sample is

probing a larger galaxy mass range than the SDSS studies, going from low-mass dwarf irregulars to giant spirals. As pointed out in the study by Lee et al. (2006), this is important for constraining the scenarios for galaxy formation and evolution. (We realize that in Lee et al. 2006 the stellar masses of some of the dwarf irregulars overlapping with our sample are significantly smaller than the masses given by Woo et al. 2008, which we use for Figure 16. This will require further investigation.) In future work, we plan to enlarge the sample of galaxies with quantitative studies of BSGs to make this comparison more significant.

8. DISTANCE

The FGLR is a tight correlation between the flux-weighted gravity ($g_F \equiv g/T_{\text{eff}}^4$, T_{eff} in units of 10^4 K) and the absolute bolometric magnitude M_{bol} of BA supergiants. As described in detail in Kudritzki et al. (2003, 2008), the physical background for this relationship is the fact that massive stars evolve at constant luminosity and mass across the HRD from the hot main sequence to the red supergiant stage. During this evolution, g_F remains constant, because of the constant luminosity and mass. On the other hand, stellar luminosity is a strong function of stellar mass (see Figure 14 as an example) and, therefore, also a strong function of flux-weighted gravity, which establishes the FGLR. (For all details, we refer the reader to the two papers just cited.) Urbaneja et al. (2008) and U et al. (2009) were the first to use the FGLR for distance determination of the metal-poor dwarf galaxy WLM and M33, respectively. Here, we follow the same procedure as was detailed in these papers.

The FGLR has the form

$$M_{\text{bol}} = a(\log g_F - 1.5) + b, \quad (5)$$

with the recent calibration provided by Kudritzki et al. (2008), $a = 3.41$ and $b = -8.02$.

For each of our targets the spectroscopic analysis yields de-reddened apparent bolometric magnitude m_{bol} and flux-weighted gravity, which are given in Table 2. These data are plotted in Figure 17. Very obviously, there is a clear relationship between flux-weighted gravity and apparent bolometric magnitude. We can use these data to fit a regression of the form

$$m_{\text{bol}} = a(\log g_F - 1.5) + b_{\text{M81}}. \quad (6)$$

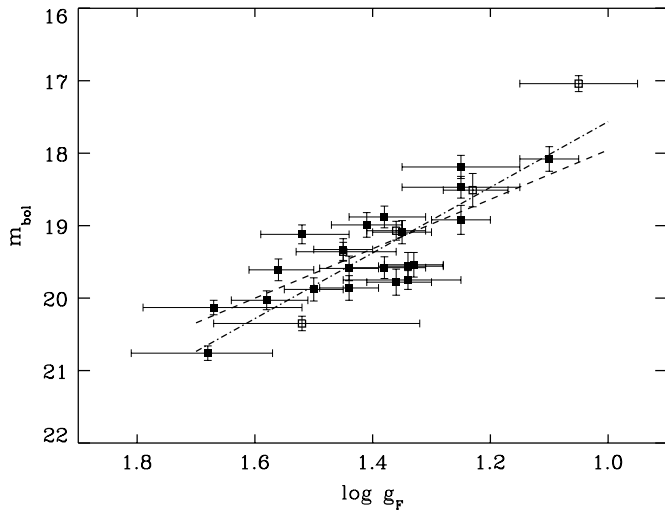


Figure 17. Observed FGLR in M81. Solid squares are targets used for the distance determination fit. Targets plotted as open squares were not included in the fit for reasons explained in the text. The dashed line corresponds to the FGLR calibration by Kudritzki et al. (2008). The dashed-dotted line is the new (still preliminary) LMC calibration (M. A. Urbaneja et al. 2012, in preparation) discussed in the text. Both calibrations yield a very similar distance modulus.

The fit result is also shown in Figure 17. Since our targets span only a limited range in g_F compared with the Kudritzki et al. (2008) calibration sample, we adopt the slope value provided by this calibration and fit only the intercept b_{M81} . The difference between b and b_{M81} yields the distance modulus, which we determine to be $\mu = 27.71 \pm 0.08$ mag (the error is calculated similarly as in Urbaneja et al. 2008).

The Kudritzki et al. (2008) calibration of the FGLR is based on data from eight galaxies with distances mostly determined from using Cepheids. Recently, we have started the study of a large sample of BA supergiants in the LMC using high-resolution, high-S/N spectra with the goal to provide a new calibration of the FGLR based on the LMC only. This work is almost completed and will be published soon (M. A. Urbaneja et al. 2012, in preparation). With an adopted distance modulus to the LMC of $m - M = 18.50$ mag we obtain the calibration values $a_{LMC} = 4.53$ and $b_{LMC} = -7.88$. While this is a significantly steeper FGLR at the low-luminosity/high- g_F end, this change in calibration does barely affect our distance determination, because most of our targets are at lower g_F /higher luminosity. A regression fit with these (still preliminary) calibration values yields a distance modulus of $\mu = 27.68 \pm 0.09$ mag. We thus adopt a distance modulus of $\mu = 27.7 \pm 0.1$ mag.

We compare this value with previous distance determinations based on Cepheids. In addition to the HST Key Project work on M81 (Freedman et al. 1994, 2001), there are two recent studies by McCommas et al. (2009) and by Gerke et al. (2011). Cepheid distance studies typically apply the Wesenheit method (Madore 1982) with a combination of V - and I -band magnitudes that is assumed to be reddening free and then compare with the corresponding period–luminosity relationship of LMC Cepheids. Following Kennicutt et al. (1998), distances are corrected for the difference in abundance between the target Cepheids and those in the LMC. This so-called metallicity correction has the form $\Delta\mu = \gamma([\text{O}/\text{H}] - 8.5)$, where $[\text{O}/\text{H}] = 12 + \log(\text{O}/\text{H})$ is the logarithmic oxygen abundance of the young stellar population in the target galaxy at the galactocentric distance of the observed Cepheid field relative to hydrogen. γ is a fit parameter and has been determined by Kennicutt et al.

(1998) from the fact that Cepheids in inner fields of the spiral galaxy M101 are brighter and yield a shorter apparent distance modulus than those in outer fields. Attributing this difference to a metallicity dependence of the period–luminosity relationship and adopting stellar metallicities and metallicity gradients from the oxygen HII region strong-line studies by Zaritsky et al. (1994), Kennicutt et al. (1998) obtained $\gamma = -0.29$ mag dex $^{-1}$. $[\text{O}/\text{H}] = 8.5$ dex in this metallicity correction is the adopted value of this abundance for the LMC. It refers to the “old” oxygen abundance scale where $[\text{O}/\text{H}]_{\odot} = 8.9$ dex. (We will show below that this value is too high independent of the actual value of the oxygen abundance for the Sun.) Macri et al. (2006) found a similar value of γ for the maser galaxy NGC 4258 again from the different distance moduli obtained from inner and outer field Cepheids.

McCommas et al. (2009) in their Cepheid distance investigation of M81 use *HST* light curves of 11 fundamental and two first-overtone short-period Cepheids in the outer disk of M81 at $R = 1.23R_{25}$ ($\simeq 13.5$ kpc) and obtain a distance modulus of M81 relative to the LMC of $\Delta\mu = 9.34 \pm 0.05$ mag. Checking the consistency with the 25 long-period Cepheids in two inner *HST* WFPC fields observed by the Key Project located at $R = 0.36R_{25}$ ($\simeq 4.3$ kpc), McCommas et al. (2009) use the same Wesenheit formalism and obtain a distance modulus 0.23 mag shorter. Following the work by Kennicutt et al. (1998) and Macri et al. (2006), they also apply a metallicity correction with $\gamma = -0.29$ mag dex $^{-1}$. This correction introduces a small increase of the distance to $\Delta\mu = 9.37 \pm 0.05$ mag and reduces the difference in distance modulus between outer and inner field Cepheids to 0.09 mag. It is based on the metallicity study by Zaritsky et al. (1994), who obtained $[\text{O}/\text{H}] = 9.196 - 0.49 R/R_{25}$ for the oxygen abundance as a function of galactocentric distance as a result of their strong-line analysis of HII region emission lines. Explaining the full difference in distance modulus between inner and outer field Cepheids in terms of metallicity with the Zaritsky et al. (1994) metallicity gradient requires $\gamma = -0.55$ mag dex $^{-1}$.

Gerke et al. (2011) investigate 107 long-period Cepheids observed with the Large Binocular Telescope in a galactocentric range of $0.29 \leq R/R_{25} \leq 0.88$ and with ground-based B , V , I photometry. Without applying a metallicity correction they obtain $\Delta\mu = 9.19 \pm 0.05$ mag. They also realize a trend in Cepheid distance modulus as a function of galactocentric distance and obtain a metallicity correction, which leads to $\gamma = -0.56 \pm 0.36$ mag dex $^{-1}$ and a distance modulus of $\Delta\mu = 9.39 \pm 0.14$ mag. This agrees with McCommas et al. (2009) and also with the original value of the Key Project of $\Delta\mu = 9.30 \pm 0.15$ mag.

Our FGLR distance to M81 is based on an LMC distance modulus of 18.5 mag and, thus, a difference of $\Delta\mu = 9.2 \pm 0.1$ mag. This is 0.10–0.19 mag or 5%–8% shorter than the ones obtained with the Cepheid work. However, we note that there is good agreement with the inner field long-period Cepheids, when no metallicity corrections are applied. In the following we discuss some aspects of this metallicity correction.

With the solar oxygen abundance $[\text{O}/\text{H}]_{\odot} = 8.69$ dex (Allende Prieto et al. 2001) the Zaritsky et al. (1994) logarithmic oxygen abundances relative to the Sun are $[\text{O}] \equiv [\text{O}/\text{H}] - [\text{O}/\text{H}]_{\odot} = 0.506 - 0.49 R/R_{25}$. If oxygen is taken as proxy for metallicity, this is a significantly higher metallicity than found in our BSG spectroscopy in Equation (4), while our gradient is shallower. Applying our metallicity gradient to correct for distance modulus difference between the inner and outer field

Cepheids in M81 would require an even more negative value of γ , namely, $\gamma = -0.65 \text{ mag dex}^{-1}$. Moreover, the LMC oxygen abundance $[\text{O}/\text{H}]_{\text{LMC}} = 8.50 \text{ dex}$ or $[\text{O}]_{\text{LMC}} = -0.19 \text{ dex}$ adopted in these corrections is too large compared with the LMC oxygen abundance of B stars found by Hunter et al. (2007) ($[\text{O}/\text{H}]_{\text{LMC}} = 8.33 \text{ dex}$ or $[\text{O}]_{\text{LMC}} = -0.36 \text{ dex}$), the iron abundances of LMC Cepheids determined by Romaniello et al. (2008) and Luck et al. (1998) ($[\text{Fe}]_{\text{LMC}} = -0.33 \text{ dex}$), and the LMC H II region oxygen abundances obtained by Bresolin (2011) ($[\text{O}/\text{H}]_{\text{LMC}} = 8.36 \text{ dex}$ or $[\text{O}]_{\text{LMC}} = -0.33 \text{ dex}$). This means that with our BSG metallicity values in M81 the Cepheids in the outer field have a metallicity 0.11 dex higher than the LMC. If one would apply the metallicity correction with $\gamma = -0.65 \text{ mag dex}^{-1}$ accordingly, this would enlarge the distance modulus by another 0.07 mag.

However, with such a large negative value of γ it is important to note that this empirical correction for the metallicity dependence of the period–luminosity relationship, which claims that Cepheids become brighter with increasing metallicity, is in striking disagreement with pulsation theory, which predicts exactly the opposite, namely, that the Cepheid brightness decreases with increasing metallicity (Fiorentino et al. 2002, 2007; Marconi et al. 2005; Bono et al. 2008). It also disagrees with the recent high-S/N, high spectral resolution quantitative spectroscopy in the Milky Way and the LMC carried out by Romaniello et al. (2008), which confirms the prediction by pulsation theory. According to this work, the value of γ should be positive and not negative. In other words, as careful spectroscopic metallicity studies compared with observed differences of distance moduli between inner and outer field Cepheids push γ to increasingly negative values, an explanation of that distance modulus difference in terms of metallicity seems unlikely. It must be something else, and it is an additional systematic effect not understood.

We also note that U et al. (2009) have demonstrated from their quantitative spectroscopy of BSGs in M33 that the difference of distance moduli between inner field and outer field Cepheids found by Scowcroft et al. (2009) would require a γ -value of $-0.55 \text{ mag dex}^{-1}$. Even worse, Bresolin et al. (2010) re-determined H II region abundances in M33 using auroral lines, and applying their abundance gradient to the Cepheid fields in M33 yields $\gamma = -1.2 \text{ mag dex}^{-1}$ (see discussion in Bresolin 2011).

Another galaxy where the comparison of Cepheids in the inner and outer fields leads to a significantly different distance modulus is the maser galaxy NGC 4258. This galaxy is of particular importance, since it has been used as the new anchor point for the extragalactic distance scale by Riess et al. (2009a, 2009b, 2011) because of its accurately known distance from the Keplerian motion of water masers orbiting the central black hole (Humphreys et al. 2008). However, Macri et al. (2006), who carried out the *HST* observations of Cepheids in NGC 4258, again found the distance modulus of the inner field Cepheids to be shorter than in the outer fields and based on the H II region strong-line method oxygen abundances by Zaritsky et al. (1994) derived a γ -value of $-0.29 \text{ mag dex}^{-1}$. Most recently, Bresolin (2011) re-determined the H II region metallicities in this galaxy, including the observation of auroral lines in a few cases. This led to a downward substantial revision of the metallicity, which seems to be close to the LMC and not strongly supersolar, and a very shallow abundance gradient. Based on these results, Bresolin (2011) shows that $\gamma = -0.69 \text{ mag dex}^{-1}$ would be needed to explain the distance modulus difference between inner and outer fields, again a value

much too negative, when compared with pulsation theory and observational work on Milky Way and LMC Cepheids. While the improved H II region work on this important galaxy still awaits an independent confirmation through a study of BSGs, it is an additional clear indication of a systematic effect on Cepheid distance moduli not understood at this point. Majaess et al. (2011) discuss the large metallicity corrections suggested by Gerke et al. (2011) and by the recent *HST/ACS* Cepheid study of M101 by Shappee & Stanek (2011) and demonstrate that such corrections lead to very improbable distances of the LMC and SMC. The work by Storm et al. (2011) indicates that a lower limit for γ is $-0.2 \text{ mag dex}^{-1}$. Majaess et al. (2011) argue that crowding is very likely responsible for the distance modulus differences obtained between inner and outer field Cepheids and not metallicity. We think that a careful spectroscopic investigation of galactic metallicities and their gradients and distance determinations using the FGLR as an independent method will help to clarify the situation.

Independent of the Cepheid work there have been numerous studies of *HST* CMDs of M81 to determine a distance from the TRGB. The distance moduli found were 28.03 mag (Sakai et al. 2004), 27.93 mag (Tikhonov et al. 2005), 27.70 mag (Rizzi et al. 2007), 27.72–27.78 mag (Dalcanton et al. 2009, different fields in the halo and the outer disk), 27.81 mag (Extragalactic Distance Database catalog; Tully et al. 2009), and 27.86 mag (Durrell et al. 2010). The more recent work since 2007 has converged on an improved methodology and seems to agree, within the uncertainties, with the distance modulus found in our study.

9. CONCLUSIONS AND FUTURE WORK

In this paper, we have demonstrated that the quantitative spectroscopy of BSGs is a promising tool to constrain the chemical evolution of galaxies and to determine their distances, which can be applied to galaxies clearly beyond the Local Group. Using the relationship between flux-weighted gravity and luminosity, we were able to determine a new distance to M81, which compares well with TRGB distances. While there is also agreement with *HST* Cepheid distances within the error margins, our results with regard to metallicity and metallicity gradient confirmed previous studies that the systematic differences between distance moduli obtained from inner and outer field Cepheids (found in M33, M81, M101, NGC 4258) are very likely not caused by a metallicity dependence of the period–luminosity relationship of Cepheids. There must be another reason for these systematic differences.

An independent check of distances obtained with either the TRGB or Cepheids is important for future work. We note that besides the importance for characterizing the physics of galaxies in the Local Volume, accurate distances and a careful discussion of the systematics of stellar distance determination methods are crucial for constraining the dark energy equation-of-state parameter $w = p/(\rho c^2)$. As is well known (Macri et al. 2006), the determination of cosmological parameters from the cosmic microwave background is affected by degeneracies in parameter space and cannot provide strong constraints on the value of H_0 (Spergel 2006; Tegmark et al. 2004). Only if additional assumptions are made, for instance, that the universe is flat, can H_0 be predicted with high precision (i.e., 2%) from the observations of the cosmic microwave background, baryonic acoustic oscillations, and type I high-redshift supernovae. If these assumptions are relaxed, then much larger uncertainties are introduced (Spergel et al. 2007; Komatsu et al. 2009). The

uncertainty of the determination of w is related to the uncertainty of H_0 through $\Delta w/w \approx 2\Delta H_0/H_0$. Thus, an independent determination of H_0 with an accuracy of 5% will allow the uncertainty of w to be reduced to ± 0.1 . While extremely promising steps toward this goal have been made by Macri et al. (2006) and Riess et al. (2009a, 2009b, 2011) using the maser galaxy NGC 4258 as a new anchor point and *HST* IR Cepheid photometry of recent Type Ia supernova galaxies out to 30 Mpc, it is clear that the complexity of this approach requires additional and independent tests. Crucial contributions that can be made using BSGs besides independent distance determinations are to investigate the role of metallicity and interstellar extinction.

We have also shown that the determination of metallicities for individual supergiant stars beyond the Local Group is possible. In this way, we can determine galaxy metallicities and metallicity gradients avoiding the systematic uncertainties of H II region strong-line methods. This can be used as an independent way to directly measure the mass–metallicity relationship of galaxies and to correlate metallicity gradients with galactic properties such as mass, angular momentum, and morphological type. But it can also be used to find out about systematic uncertainties of H II region strong-line method calibrations and to identify the more reliable ones or to develop a new one tested with BSG metallicities. Moreover, in combination with metallicity information of an older population of stars obtained through the analysis of CMDs or the spectroscopy of PNe the chemical evolution history of galaxies can be investigated. In the case of the disk of M81 we have found an indication of a late enrichment of heavy elements, which is significantly different from the Milky Way. We have also provided the first mass–metallicity relationship for star-forming galaxies solely based on stellar spectroscopy.

This work was supported by the National Science Foundation under grant AST-1008798 to R.P.K. and F.B. Moreover, R.P.K. acknowledges support by the Alexander-von-Humboldt Foundation and the hospitality of the Max-Planck-Institute for Astrophysics in Garching and the University Observatory Munich, where part of this work was carried out. W.G. and G.P. gratefully acknowledge financial support for this work from the Chilean Center for Astrophysics FONDAF 15010003 and from the BASAL Centro de Astrofísica y Tecnologías Afines (CATA) PFB-06/2007. All members of our team want to thank the Keck staff astronomers for their dedicated first-class professional support, when the observations were planned and carried out. Last but not least, we also acknowledge the use of the Hyperleda database (<http://leda.univ-lyon1.fr>).

We acknowledge the discussion of this work with Drs. Lucas Macri, Richard Henry, and Ortwin Gerhard. Most importantly, we thank our anonymous referee for the extremely careful review of the manuscript and for many very helpful suggestions to improve this paper.

The data presented in this work were obtained at the W. M. Keck Observatory, which is operated as a scientific partnership among the California Institute of Technology, the University of California, and the National Aeronautics and Space Administration. The Observatory was made possible by the generous financial support of the W. M. Keck Foundation.

The authors recognize and acknowledge the very significant cultural role and reverence that the summit of Mauna Kea has always had within the indigenous Hawaiian community. We are most fortunate to have the opportunity to conduct observations from this mountain.

Facilities: Keck:I, HST (ACS)

REFERENCES

- Allende Prieto, C., Lambert, D. L., & Asplund, M. 2001, *ApJ*, **556**, L63
- Appleton, P. N., Davies, R. D., & Stephenson, R. J. 1981, *MNRAS*, **195**, 327
- Barker, M. K., Ferguson, A. M. N., Irwin, M., Arimoto, N., & Jablonka, P. 2009, *AJ*, **138**, 1469
- Bèland, S., Boulade, O., & Davidge, T. 1988, Bulletin d'information du telescope Canada–France–Hawaii, **19**, 16
- Bono, G., Caputo, F., Fiorentino, G., Marconi, M., & Musella, I. 2008, *ApJ*, **684**, 102
- Bresolin, F. 2003, in *Stellar Candles for the Extragalactic Distance Scale*, ed. D. Alloin & W. Gieren (Lecture Notes in Physics, 635; Berlin: Springer), 149
- Bresolin, F. 2011, *ApJ*, **729**, 56
- Bresolin, F., Gieren, W., Kudritzki, R.-P., et al. 2009, *ApJ*, **700**, 309
- Bresolin, F., Pietrzyński, G., Gieren, W., & Kudritzki, R. P. 2005, *ApJ*, **634**, 1020
- Bresolin, F., Pietrzyński, G., Urbaneja, M. A., et al. 2006, *ApJ*, **648**, 1007
- Bresolin, F., Stasińska, G., Vílchez, J. M., Simon, J. D., & Rosolowsky, E. 2010, *MNRAS*, **404**, 1679
- Bresolin, F., Urbaneja, M. A., Gieren, W., Pietrzyński, G., & Kudritzki, R.-P. 2007, *ApJ*, **671**, 2028
- Brooks, A. M., Governato, F., Booth, C. M., et al. 2007, *ApJ*, **655**, L17
- Cardelli, J. A., Clayton, G. C., & Mathis, J. S. 1989, *ApJ*, **345**, 245
- Chandar, R., Ford, H. C., & Tsvetanov, Z. 2001, *AJ*, **122**, 1330
- Chemin, L., Carignan, C., & Foster, T. 2009, *ApJ*, **705**, 1395
- Chiappini, C., Matteucci, F., & Romano, D. 2001, *ApJ*, **554**, 1044
- Colavitti, E., Matteucci, F., & Murante, G. 2008, *A&A*, **483**, 401
- Daflon, S., & Cunha, K. 2004, *ApJ*, **617**, 1115
- Dalcanton, J. J., Williams, B. F., Seth, A. C., et al. 2009, *ApJS*, **183**, 67
- Davé, R., Finlator, K., & Oppenheimer, B. D. 2011a, *MNRAS*, **416**, 1354
- Davé, R., Oppenheimer, B. D., & Finlator, K. 2011b, *MNRAS*, **415**, 11
- Davidge, T. J. 2009, *ApJ*, **697**, 1439
- de Blok, W. J. G., Walter, F., Brinks, E., et al. 2008, *AJ*, **136**, 2648
- De Lucia, G., Kauffmann, G., & White, S. D. M. 2004, *MNRAS*, **349**, 1101
- de Rossi, M. E., Tissera, P. B., & Scannapieco, C. 2007, *MNRAS*, **374**, 323
- Denicoló, G., Terlevich, R., & Terlevich, E. 2002, *MNRAS*, **330**, 69
- Durrell, P. R., Sarajedini, A., & Chandar, R. 2010, *ApJ*, **718**, 1118
- Evans, C. J., Bresolin, F., Urbaneja, M. A., et al. 2007, *ApJ*, **659**, 1198
- Finlator, K., & Davé, R. 2008, *MNRAS*, **385**, 2181
- Fiorentino, G., Caputo, F., Marconi, M., & Musella, I. 2002, *ApJ*, **576**, 402
- Fiorentino, G., Marconi, M., Musella, I., & Caputo, F. 2007, *A&A*, **476**, 863
- Freedman, W. L., Hughes, S. M., Madore, B. F., et al. 1994, *ApJ*, **427**, 628
- Freedman, W. L., Madore, B. F., Gibson, B. K., et al. 2001, *ApJ*, **553**, 47
- Fuhrmann, K. 2011, *MNRAS*, **414**, 2893
- Garnett, D. R. 2004, in *Cosmochemistry, The Melting Pot of the Elements*, ed. C. Esteban, R. J. García López, A. Herrero, & F. Sánchez (Cambridge: Cambridge Univ. Press), 171
- Garnett, D. R., & Shields, G. A. 1987, *ApJ*, **317**, 82
- Garnett, D. R., Shields, G. A., Skillman, E. D., Sagan, S. P., & Dufour, R. J. 1997, *ApJ*, **489**, 63
- Gerke, J. R., Kochanek, C. S., Prieto, J. L., Stanek, K. Z., & Macri, L. M. 2011, *ApJ*, **743**, 176
- Grevesse, N., & Sauval, A. J. 1998, *Space Sci. Rev.*, **85**, 161
- Heckman, T. M., Armus, L., & Miley, G. K. 1990, *ApJS*, **74**, 833
- Henry, R. B. C., & Howard, J. W. 1995, *ApJ*, **438**, 170
- Henry, R. B. C., Kwitter, K. B., Jaskot, A. E., et al. 2010, *ApJ*, **724**, 748
- Herrero, A., Kudritzki, R. P., Vílchez, J. M., et al. 1992, *A&A*, **261**, 209
- Horne, K. 1986, *PASP*, **98**, 609
- Hou, J. L., Prantzos, N., & Boissier, S. 2000, *A&A*, **362**, 921
- Humphreys, E. M. L., Reid, M. J., Greenhill, L. J., Moran, J. M., & Argon, A. L. 2008, *ApJ*, **672**, 800
- Hunter, I., Dufton, P. L., Smartt, S. J., et al. 2007, *A&A*, **466**, 277
- Kaufer, A., Venn, K. A., Tolstoy, E., Pinte, C., & Kudritzki, R.-P. 2004, *AJ*, **127**, 2723
- Kennicutt, R. C., Jr., Stetson, P. B., Saha, A., et al. 1998, *ApJ*, **498**, 181
- Kent, S. M. 1987, *AJ*, **93**, 816
- Kewley, L. J., & Dopita, M. A. 2002, *ApJS*, **142**, 35
- Kewley, L. J., & Ellison, S. L. 2008, *ApJ*, **681**, 1183
- Kobulnicky, H. A., & Kewley, L. J. 2004, *ApJ*, **617**, 240
- Komatsu, E., Dunkley, J., Nolte, M. R., et al. 2009, *ApJS*, **180**, 330
- Köppen, J., Weidner, C., & Kroupa, P. 2007, *MNRAS*, **375**, 673
- Kudritzki, R. P., Bresolin, F., & Przybilla, N. 2003, *ApJ*, **582**, L83
- Kudritzki, R. P., & Urbaneja, M. A. 2009, in *Massive Stars: From Pop III and GRBs to the Milky Way*, ed. M. Livio & E. Villaver (Space Telescope Science Institute Symposium Series No. 20; Cambridge: Cambridge Univ. Press), 126
- Kudritzki, R.-P., Urbaneja, M. A., Bresolin, F., et al. 2008, *ApJ*, **681**, 269

- Lee, H., Skillman, E. D., Cannon, J. M., et al. 2006, *ApJ*, **647**, 970
- Lequeux, J., Peimbert, M., Rayo, J. F., Serrano, A., & Torres-Peimbert, S. 1979, *A&A*, **80**, 155
- Luck, R. E., Andrievsky, S. M., Kovtyukh, V. V., Gieren, W., & Graczyk, D. 2011, *AJ*, **142**, 51
- Luck, R. E., Kovtyukh, V. V., & Andrievsky, S. M. 2006, *AJ*, **132**, 902
- Luck, R. E., Moffett, T. J., Barnes, T. G., & Gieren, W. 1998, *AJ*, **115**, 605
- Maciel, W. J., & Costa, R. D. D. 2009, in IAU Symp., 254, The Galaxy Disk in Cosmological Context, ed. J. Andersen, J. Bland-Hawthorn, & B. Nordström (Cambridge: Cambridge Univ. Press), 38P
- Maciel, W. J., Costa, R. D. D., & Idiart, T. E. P. 2010, *A&A*, **512**, A19
- Macri, L. M., Stanek, K. Z., Bersier, D., Greenhill, L. J., & Reid, M. J. 2006, *ApJ*, **652**, 1133
- Madore, B. F. 1982, *ApJ*, **253**, 575
- Maiolino, R., Nagao, T., Grazian, A., et al. 2008, *A&A*, **488**, 463
- Majaess, D., Turner, D., & Gieren, W. 2011, *ApJ*, **741**, L36
- Marconi, M., Musella, I., & Fiorentino, G. 2005, *ApJ*, **632**, 590
- Martin, C. L. 1997, *ApJ*, **491**, 561
- McCommas, L. P., Yoachim, P., Williams, B. F., et al. 2009, *AJ*, **137**, 4707
- McGaugh, S. S. 1991, *ApJ*, **380**, 140
- Meynet, G., & Maeder, A. 2003, *A&A*, **404**, 975
- Mould, J., & Sakai, S. 2008, *ApJ*, **686**, L75
- Mould, J., & Sakai, S. 2009, *ApJ*, **697**, 996
- Naab, T., & Ostriker, J. P. 2006, *MNRAS*, **366**, 899
- Oke, J. B. 1990, *AJ*, **99**, 1621
- Oke, J. B., Cohen, J. G., Carr, M., et al. 1995, *PASP*, **107**, 375
- Pagel, B. E. J., Edmunds, M. G., Blackwell, D. E., Chun, M. S., & Smith, G. 1979, *MNRAS*, **189**, 95
- Paturel, G., Petit, C., Prugniel, P., et al. 2003, *A&A*, **412**, 45
- Pettini, M., & Pagel, B. E. J. 2004, *MNRAS*, **348**, L59
- Pilyugin, L. S. 2001, *A&A*, **374**, 412
- Pilyugin, L. S., & Thuan, T. X. 2005, *ApJ*, **631**, 231
- Prantzos, N., & Boissier, S. 2000, *MNRAS*, **313**, 338
- Press, W. H., Teukolsky, S. A., Vetterling, W. T., & Flannery, B. P. 1992, in Numerical Recipes (2nd ed.; Cambridge: Cambridge Univ. Press)
- Przybilla, N., Butler, K., Becker, S. R., & Kudritzki, R. P. 2006, *A&A*, **445**, 1099
- Przybilla, N., Butler, K., & Kudritzki, R.-P. 2008a, in The Metal-Rich Universe, ed. G. Israelian & G. Meynet (Cambridge: Cambridge Univ. Press), 332
- Przybilla, N., Nieva, M. F., Heber, U., & Butler, K. 2008b, *ApJ*, **684**, L103
- Riess, A. G., Macri, L., Casertano, S., et al. 2009a, *ApJ*, **699**, 539
- Riess, A. G., Macri, L., Casertano, S., et al. 2011, *ApJ*, **730**, 119
- Riess, A. G., Macri, L., Li, W., et al. 2009b, *ApJS*, **183**, 109
- Rizzi, L., Tully, R. B., Makarov, D., et al. 2007, *ApJ*, **661**, 815
- Rolleston, W. R. J., Smartt, S. J., Dufton, P. L., & Ryans, R. S. I. 2000, *A&A*, **363**, 537
- Romaniello, M., Primas, F., Mottini, M., et al. 2008, *A&A*, **488**, 731
- Roškar, R., Debattista, V. P., Quinn, T. R., Stinson, G. S., & Wadsley, J. 2008, *ApJ*, **684**, L79
- Sakai, S., Ferrarese, L., Kennicutt, R. C., Jr., & Saha, A. 2004, *ApJ*, **608**, 42
- Sánchez-Blázquez, P., Courty, S., Gibson, B. K., & Brook, C. B. 2009, *MNRAS*, **398**, 591
- Santiago-Cortés, M., Mayya, Y. D., & Rosa-González, D. 2010, *MNRAS*, **405**, 1293
- Schiller, F. 2010, thesis, Friedrich-Alexander-University Erlangen-Nuernberg, Germany
- Schiller, F., & Przybilla, N. 2008, *A&A*, **479**, 849
- Schlegel, D. J., Finkbeiner, D. P., & Davis, M. 1998, *ApJ*, **500**, 525
- Scowcroft, V., Bersier, D., Mould, J. R., & Wood, P. R. 2009, *MNRAS*, **396**, 1287
- Shappee, B. J., & Stanek, K. Z. 2011, *ApJ*, **733**, 124
- Skillman, E. D. 1998, in Stellar Astrophysics for the Local Group: VIII Canary Islands Winter School of Astrophysics, ed. A. Aparicio, A. Herrero, & F. Sanchez (Cambridge: Cambridge Univ. Press), 457
- Smartt, S. J., Crowther, P. A., Dufton, P. L., et al. 2001, *MNRAS*, **325**, 257
- Sofue, Y., Honma, M., & Omodaka, T. 2009, *PASJ*, **61**, 227
- Spergel, D. 2006, APS April Meeting Abstracts, 5002
- Spergel, D. N., Bean, R., Doré, O., et al. 2007, *ApJS*, **170**, 377
- Stanghellini, L., & Haywood, M. 2010, *ApJ*, **714**, 1096
- Stanghellini, L., Magrini, L., Villaver, E., & Galli, D. 2010, *A&A*, **521**, A3
- Stauffer, J. R., & Bothun, G. D. 1984, *AJ*, **89**, 1702
- Storm, J., Gieren, W., Fouque, P., et al. 2011, *A&A*, **534**, A95
- Tegmark, M., Strauss, M. A., Blanton, M. R., et al. 2004, *Phys. Rev. D*, **69**, 103501
- Tikhonov, N. A., Galazutdinova, O. A., & Drozdovsky, I. O. 2005, *A&A*, **431**, 127
- Tremonti, C. A., Heckman, T. M., Kauffmann, G., et al. 2004, *ApJ*, **613**, 898
- Trundle, C., Dufton, P. L., Lennon, D. J., Smartt, S. J., & Urbaneja, M. A. 2002, *A&A*, **395**, 519
- Trundle, C., & Lennon, D. J. 2005, *A&A*, **434**, 677
- Tully, R. B., Rizzi, L., Shaya, E. J., et al. 2009, *AJ*, **138**, 323
- U, V., Urbaneja, M. A., Kudritzki, R.-P., et al. 2009, *ApJ*, **704**, 1120
- Urbaneja, M. A., Herrero, A., Bresolin, F., et al. 2005a, *ApJ*, **622**, 862
- Urbaneja, M. A., Herrero, A., Kudritzki, R. P., et al. 2005b, *ApJ*, **635**, 311
- Urbaneja, M. A., Kudritzki, R.-P., Bresolin, F., et al. 2008, *ApJ*, **684**, 118
- Venn, K. A., Lennon, D. J., Kaufer, A., et al. 2001, *ApJ*, **547**, 765
- Wiersma, R. P. C., Schaye, J., & Smith, B. D. 2009, *MNRAS*, **393**, 99
- Williams, B. F., Dalcanton, J. J., Seth, A. C., et al. 2009, *AJ*, **137**, 419
- Woo, J., Courteau, S., & Dekel, A. 2008, *MNRAS*, **390**, 1453
- Yin, J., Hou, J. L., Prantzos, N., et al. 2009, *A&A*, **505**, 497
- Zaritsky, D., Kennicutt, R. C., Jr., & Huchra, J. P. 1994, *ApJ*, **420**, 87